Markov chain Monte Carlo analysis to probe trilinear *R*-parity violating SUSY scenarios and possible LHC signatures

Arghya Choudhury,[1,*] Sourav Mitra,[2,†] Arpita Mondal,[1,‡] and Subhadeep Mondal[3,§]

[1]*Department of Physics, Indian Institute of Technology Patna, Bihar, 801106, India*
[2]*Surendranath College, 24/2 M. G. Road, Kolkata, West Bengal, 700009, India*
[3]*Department of Physics, SEAS, Bennett University, Greater Noida, Uttar Pradesh, 201310, India*

(Received 6 January 2025; accepted 18 June 2025; published 18 July 2025)

In this article, we probe the trilinear *R*-parity violating (RPV) supersymmetric (SUSY) scenarios with specific nonzero interactions in the light of neutrino oscillation, Higgs, and flavor observables. We attempt to fit the set of observables using a state-of-the-art Markov Chain Monte Carlo (MCMC) setup and study its impact on the model parameter space. Our main objective is to constrain the trilinear couplings individually, along with some other SUSY parameters relevant to the observables. We present the constrained parameter regions in the form of marginalized posterior distributions on different two-dimensional parameter planes. We perform our analyses with two different scenarios characterized by our choices for the lightest SUSY particle (LSP), bino, and stop. Our results indicate that the lepton number violating trilinear couplings λ_{i33} ($i = 1, 2$) and λ'_{j33} ($j = 1, 2, 3$) can be at most of the order of 10^{-4} or even smaller while $\tan\beta$ is restricted to below 15 even when 3σ allowed regions are considered. We further comment on the possible LHC signatures of these LSPs focusing on and around the best-fit regions.

DOI: 10.1103/r6v9-nck7

I. INTRODUCTION

Neutrino oscillation data from several experiments [1–8] provides some of the strongest evidence for the existence of beyond the standard model (BSM) physics. The mass-squared differences and mixing angles measured by neutrino oscillation experiments indicate that at least two light neutrino masses are nonzero, along with significant mixing among the three flavor states. Standard model (SM) [9–12] as well as the *R*-parity [13] conserving minimal supersymmetric (SUSY) standard model (MSSM) [13–15] cannot explain the generation of light neutrino masses and mixings. However, *R* parity happens to be a discrete symmetry that is imposed on MSSM to ensure the stability of the lightest supersymmetric particle (LSP) and does not follow from any fundamental principle. A more generic version of the MSSM, therefore, contains *R*-parity violating (RPV) terms [13,16–18], which can lead to generation of light neutrino masses and mixings naturally [16,19–23].

Unlike *R*-parity conserving scenarios, RPV scenarios are yet to be studied exhaustively. It would be of particular interest to see how much of its sub-TeV parameter space can be constrained from existing data from neutrino oscillation as well as precision Higgs data and collider limits on SUSY particles. Four types of RPV terms can be added to the superpotential, which either violate the lepton number or the baryon number. Among these, there are three terms, one bilinear and two trilinear, that violate the lepton number by one unit, and one trilinear term, which violates the baryon number by one unit. The implication of these nonzero RPV couplings on light neutrino masses and mixings have been discussed in existing literature [16,19–28]. However, a detailed statistical analysis through posterior distributions of the RPV couplings and other relevant SUSY parameters was only performed recently with nonzero bilinear RPV couplings [29]. A similar study with trilinear lepton number violating couplings has been missing so far. Note that, whereas the bilinear RPV couplings can partially generate light neutrino masses at the tree level itself, the lowest order contributions from the trilinear couplings arise at one loop [16,19–22]. Nevertheless, a complete one-loop calculation is necessary for both scenarios.

In this work, we focus on chosen trilinear lepton number violating couplings that contribute dominantly towards light neutrino mass generation. Apart from these, we set all other

*Contact author: arghya@iitp.ac.in
†Contact author: hisourav@gmail.com
‡Contact author: arpita_1921ph15@iitp.ac.in
§Contact author: subhadeep.mondal@bennett.edu.in

Published by the American Physical Society under the terms of the Creative Commons Attribution 4.0 International license. Further distribution of this work must maintain attribution to the author(s) and the published article's title, journal citation, and DOI. Funded by SCOAP³.

RPV couplings to zero. Keeping both bilinear and trilinear lepton number violating interactions makes it easier to fit the neutrino oscillation data, with the dominating contribution arising from the bilinear terms. However, our objective here is to assess the impact of the neutrino oscillation data on lepton number violating trilinear couplings only. Note that just as one can start only with the bilinear interaction terms and generate the lepton number violating trilinear interactions [30], starting from the trilinear interaction terms through renormalization group evolution, one can also generate the bilinear terms at a different energy scale [31,32]. In addition to the RPV couplings and their corresponding soft terms, some other SUSY parameters are also relevant in this context. These include the μ parameter, $\tan\beta$, and the soft mass parameters of sleptons and squarks. Choice of these SUSY parameters can, in turn, affect the 125 GeV Higgs observables [33,34], which are also taken into account. In addition to that, B-meson decay branching ratios [35–37] that are very precisely measured and are sensitive to choice of SUSY spectrum are also considered in this study as observables. We have performed our analyses for two different LSP scenarios, namely, bino and stop. First, we consider the model with only LQD type couplings (Bino$_{\lambda'}$-model). Next, we analyze the models with both LLE and LQD couplings (Bino$_{\lambda\lambda'}$-model). Finally, we consider the stop LSP scenario, with both LLE and LQD couplings (Stop$_{\lambda\lambda'}$-model). We also comment on the impact of collider limits on SUSY particle masses in RPV context [38–45] on our results.

Given the precision of the observables used in this study and the number of input parameters, a random scan does not yield any allowed parameter space. Hence, we have adopted a Markov Chain Monte Carlo (MCMC) [46] algorithm to sample the parameter space. The objective is not only to find some allowed parameter space but to generate posterior distributions of the input parameters corresponding to 99%, 95%, and 68% confidence levels through Bayesian analysis similar to the study performed recently with only bilinear interaction terms [29]. The derived results not only give us a robust understanding of the available parameter space but also provide future directions to any phenomenological studies performed with this model.

The paper is organized as follows: In Sec. II, we discuss the generation of neutrino masses and mixing from the trilinear lepton number violating terms. We summarize the latest global fit of the neutrino oscillation data along with the constraints coming from Higgs mass, Higgs coupling strength modifiers, and the B-meson decay branching ratios in Sec. III. In Sec. IV, we review the recent collider limit on the sparticle masses coming from direct search results obtained by the ATLAS and CMS groups. The details of the MCMC analysis setup are briefly discussed in Sec. V. In Secs. VI and VII, we present the results for different trilinear RPV models considering bino and stop LSP scenarios, respectively. Lastly, we conclude in Sec. VIII.

II. MODEL DESCRIPTION

The lepton number violating terms associated with trilinear couplings in the RPV SUSY model are expressed as follows [16,47,48]:

$$W_{\not L} = \frac{1}{2}\lambda_{ijk} L_i L_j E^c_k + \lambda'_{ijk} L_i Q_j D^c_k. \tag{2.1}$$

The first term can be reformulated using $SU(2)_L$ indices as $\epsilon_{\alpha\beta} L^\alpha_i L^\beta_j E^c_k$, where $\alpha, \beta = 1, 2$. Due to the gauge invariance and presence of antisymmetric $\epsilon_{\alpha\beta}$ tensor, the λ_{ijk} couplings also become antisymmetric in the first two indices ($\lambda_{ijk} = -\lambda_{jik}$) [16] and the first term in the Eq. (2.1) can be written as $\lambda_{ijk}\hat{L}_i\hat{L}_j\hat{E}^c_k = \lambda_{ijk}\epsilon_{\alpha\beta}\hat{L}^\alpha_i\hat{L}^\beta_j\hat{E}^c_k = -\lambda_{jik}\epsilon_{\beta\alpha}\hat{L}^\alpha_j\hat{L}^\beta_i\hat{E}^c_k = -\lambda_{jik}\hat{L}_i\hat{L}_j\hat{E}^c_k$. This leads to 9 unique λ_{ijk} and 27 λ'_{ijk} lepton number violating trilinear couplings. The Lagrangian for these two terms can be represented as [16,47]

$$\begin{aligned}\mathcal{L}_{\not L} = &-\frac{\lambda_{ijk}}{2}[\tilde{\nu}_{iL}\bar{l}_{kR}l_{jL} + \tilde{l}_{jL}\bar{l}_{kR}\nu_{iL} + \tilde{l}^*_{kR}\bar{\nu}^c_{iR}l_{jL} - (i \leftrightarrow j)] \\ &- \lambda'_{ijk}[\tilde{\nu}_{iL}\bar{d}_{kR}d_{jL} + \tilde{d}_{jL}\bar{d}_{kR}\nu_{iL} + \tilde{d}^*_{kR}\bar{\nu}^c_{iR}d_{jL} - \tilde{l}_{iL}\bar{d}_{kR}u_{jL} \\ &- \tilde{u}_{jL}\bar{d}_{kR}l_{iL} - \tilde{d}^*_{kR}\bar{l}^c_{iR}u_{jL}] + \text{H.c.}\end{aligned} \tag{2.2}$$

The soft terms corresponding to the R-parity violating superpotential involving these two trilinear couplings are given by [16]

$$V^{\text{soft}}_{\not L} = \frac{1}{2}A_{ijk}\tilde{L}_i\tilde{L}_j\tilde{l}^c_k + A'_{ijk}\tilde{L}_i\tilde{Q}_j\tilde{d}^c_k + \text{H.c.} \tag{2.3}$$

The soft coupling terms also have 9 and 27 independent parameters corresponding to A_{ijk} and A'_{ijk} terms, respectively. The trilinear RPV couplings (λ and λ') and the corresponding soft coupling terms (A_{ijk} and A'_{ijk}) are related with the physical Yukawa terms as follows:

$$\begin{aligned}\lambda_{ijk} &= \sum_{\alpha,\beta} e_{\alpha i} e_{\beta j} \lambda^e_{\alpha\beta k} \qquad \lambda'_{ijk} = \sum_{\alpha} e_{\alpha i}\lambda^d_{\alpha jk} \\ A_{ijk} &= \sum_{\alpha,\beta} e_{\alpha i} e_{\beta j} A^e_{\alpha\beta k} \qquad A'_{ijk} = \sum_{\alpha} e_{\alpha i} A'^d_{\alpha jk},\end{aligned} \tag{2.4}$$

where $\lambda^e_{\alpha\beta k}$ and $\lambda^d_{\alpha jk}$ with $\alpha \equiv \beta = (0, 1, 2, 3)$[1] are physical Yukawa terms and $\vec{e}_i \equiv \{e_{\alpha i}\}_{\alpha=0,\ldots,3}$ obeys $\vec{v}\cdot\vec{e}_i = 0$ and $\vec{e}_i \cdot \vec{e}_j = \delta_{ij}$ [16]. Similarly, $A^e_{\alpha\beta k}$ and $A'^d_{\alpha jk}$ are physical terms corresponding to soft couplings. The one loop contribution to the light neutrino mass matrix arising from the λ, λ' couplings are presented in Fig. 1. These contributions can be expressed as [16,49–51]

[1]Here $\lambda^e_{0jk} = \lambda^0_{jk}$ and $\lambda^d_{0jk} = \lambda^d_{jk}$.

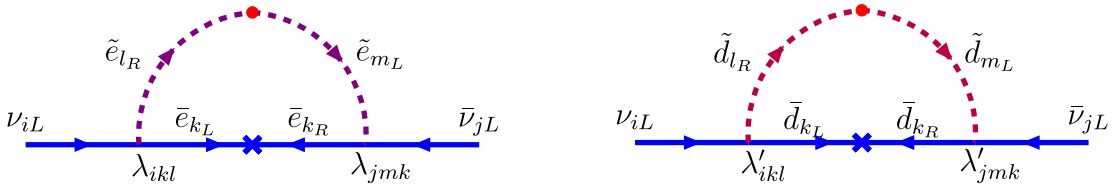


FIG. 1. The loop diagrams contributing to the light neutrino masses aided by λ couplings (left) and λ' couplings (right) are shown here. The Majorana mass and the scalar mass insertions are represented by the cross and the dot on the respective lines for neutrino and scalar sparticles (slepton and squark), respectively.

$$M^{\nu}_{ij}|_{\lambda} = \frac{1}{16\pi^2}\sum_{k,l,m}\lambda_{ikl}\lambda_{jmk}m_{e_k}\frac{(\tilde{m}^{e^2}_{LR})_{ml}}{m^2_{\tilde{e}_{Rl}}-m^2_{\tilde{e}_{Lm}}}\ln\left(\frac{m^2_{\tilde{e}_{Rl}}}{m^2\tilde{e}_{Lm}}\right) + (i\leftrightarrow j),$$
$$M^{\nu}_{ij}|_{\lambda'} = \frac{3}{16\pi^2}\sum_{k,l,m}\lambda'_{ikl}\lambda'_{jmk}m_{d_k}\frac{(\tilde{m}^{d^2}_{LR})_{ml}}{m^2_{\tilde{d}_{Rl}}-m^2_{\tilde{d}_{Lm}}}\ln\left(\frac{m^2_{\tilde{d}_{Rl}}}{m^2\tilde{d}_{Lm}}\right) + (i\leftrightarrow j). \quad (2.5)$$

The functional forms are identical except for a factor of 3 in the mass contribution coming from λ', which arises due to different color combinations. The slepton mixing term can be expressed in terms of coupling parameters as $\tilde{m}^{e^2}_{LR} = (A^e_{ij} - \mu\tan\beta\lambda^e_{ij})\frac{v_d}{\sqrt{2}}$, where all the charged lepton masses and the associated doublet and singlet mass matrices are diagonal. Similarly, for the squarks, assuming the down quark masses and their corresponding scalar doublets and singlets are diagonal, the mixing term can be expressed as $\tilde{m}^{d^2}_{LR} = (A^d_{ij} - \mu\tan\beta\lambda^e_{ij})\frac{v_d}{\sqrt{2}}$. Furthermore, under certain assumptions such as degenerate sfermion masses and A terms proportional to Yukawa couplings ($A^e_{ij} = A^e\lambda^e_{ij}$ and $A^d_{ij} = A^d\lambda^d_{ij}$), the equations in Eq. (2.5) can be reformulated as follows [16,51–53]:

$$M^{\nu}_{ij}|_{\lambda} \simeq \frac{1}{8\pi^2}\frac{A^e-\mu\tan\beta}{\bar{m}^2_{\tilde{e}}}\sum_{k,l}\lambda_{ikl}\lambda_{jkl}m_{e_k}m_{e_l},$$
$$M^{\nu}_{ij}|_{\lambda'} \simeq \frac{3}{8\pi^2}\frac{A^d-\mu\tan\beta}{\bar{m}^2_{\tilde{d}}}\sum_{k,l}\lambda'_{ikl}\lambda'_{jkl}m_{d_k}m_{d_l}. \quad (2.6)$$

Here, $\bar{m}_{\tilde{e}}$ and $\bar{m}_{\tilde{d}}$ denote the scalar mass parameters corresponding to the charged lepton and down quark mass eigenstates, respectively. Although the equations in Eq. (2.6) do not explicitly depend on A or A', but they involve a large number of independent parameters (40), including λ_{ijk} (9), λ'_{ijk} (27), μ, $\tan\beta$, $\bar{m}^2_{\tilde{e}}$, and $\bar{m}^2_{\tilde{d}}$. To simplify, one can assume that there is no strong hierarchy among λ_{ijk} and λ'_{ijk} couplings for a given index i [51,54–56]. Additionally, assuming models where fermion mass hierarchy is explained by flavor symmetries, contributions with $k,\ l = 2,\ 3$ dominate [51] in the equations in Eq. (2.6). Furthermore, setting all sfermion mass parameters ($\bar{m}^2_{\tilde{d}}$ and $\bar{m}^2_{\tilde{e}}$) as $\tilde{m}$, contributions to the light neutrino mass matrix can be expressed as [16,51–53,57]

$$M^{\nu}_{ij}|_{\lambda} \simeq \frac{1}{8\pi^2}\left\{\lambda_{i33}\lambda_{j33}\frac{m^2_{\tau}}{\tilde{m}} + (\lambda_{i23}\lambda_{j32}+\lambda_{i32}\lambda_{j23})\frac{m_{\mu}m_{\tau}}{\tilde{m}} + \lambda_{i22}\lambda_{j22}\frac{m^2_{\mu}}{\tilde{m}}\right\},$$
$$M^{\nu}_{ij}|_{\lambda'} \simeq \frac{3}{8\pi^2}\left\{\lambda'_{i33}\lambda'_{j33}\frac{m^2_{b}}{\tilde{m}} + (\lambda'_{i23}\lambda'_{j32}+\lambda'_{i32}\lambda'_{j23})\frac{m_{s}m_{b}}{\tilde{m}} + \lambda'_{i22}\lambda'_{j22}\frac{m^2_{s}}{\tilde{m}}\right\}. \quad (2.7)$$

In this pair of mass equations, a natural hierarchy emerges in fermion masses, such as $\frac{m^2_{\tau}}{m^2_{\mu}} \sim 300$ and $\frac{m^2_{b}}{m^2_{s}} \sim 600$ [16,53,57]. Consequently, our focus lies on the contributions stemming from fermions with significant masses, namely, the b quark and τ lepton. In this context, various models with diagonal and off-diagonal RPV trilinear couplings have been explored in existing literature [16,57]. In our study, we consider a simple diagonal model presented in [57], and by combining these two diagonal contributions, the final light neutrino mass matrix can be expressed as

$$M_{\nu}|_{\lambda+\lambda'} = \frac{1}{8\pi^2\tilde{m}}[\lambda_{i33}\lambda_{j33}m^2_{\tau} + 3\lambda'_{i33}\lambda'_{j33}m^2_{b}] = \frac{1}{8\pi^2\tilde{m}}M^{\nu}_{ij}, \quad (2.8)$$

where the matrix M^{ν}_{ij} has the form

$$M^{\nu}_{ij} = \begin{pmatrix} \lambda^2_{133} m^2_\tau + 3\lambda'^2_{133} m^2_b & \lambda_{133}\lambda_{233} m^2_\tau + 3\lambda'_{133}\lambda'_{233} m^2_b & 3\lambda'_{133}\lambda'_{333} m^2_b \\ \lambda_{233}\lambda_{133} m^2_\tau + 3\lambda'_{233}\lambda'_{133} m^2_b & \lambda^2_{233} m^2_\tau + 3\lambda'^2_{233} m^2_b & 3\lambda'_{233}\lambda'_{333} m^2_b \\ 3\lambda'_{333}\lambda'_{133} m^2_b & 3\lambda'_{333}\lambda'_{233} m^2_b & 3\lambda'^2_{333} m^2_b \end{pmatrix}. \tag{2.9}$$

Due to the asymmetry of the λ_{ijk} coupling, the absence of a λ_{333} term is evident in this mass matrix. The third neutrino gets mass at the leading order, and it can be approximated as [16]

$$m_{\nu_3} = \frac{3m_b^2}{8\pi^2 \tilde{m}} \sum_i \lambda'^2_{i33}. \tag{2.10}$$

III. CONSTRAINTS FROM NEUTRINO OSCILLATION, FLAVOR PHYSICS, AND HIGGS DATA

We have considered two mass square differences, namely, Δm^2_{21} and $|\Delta m^2_{31}|$ ($\Delta m^2_{i1} = m^2_i - m^2_1$, where $i = 2, 3$) along with three mixing angles (θ_{13}, θ_{12}, and θ_{23}) obtained from global fit of neutrino oscillation data. The CP violating phase δ_{CP} has not been considered in our analysis. There are still large error bars associated with measurements of CP-violating phases in neutrino oscillation experiments. For example, in the normal hierarchical scenario, the phase is consistent with π within 1σ of the best-fit value [8], which makes the scenario consistent with zero CP phase. The data corresponding to inverted hierarchy also comes with a significantly large uncertainty [8]. Adding these observables does not restrict our parameter regions any further. On the other hand, to address nonzero values of the phase angle, one is required to add additional input parameters, which makes the numerical computation even more time consuming. Hence, we have calculated the mixing angles from the PMNS matrix by putting $\delta_{CP} = 0$ [58–60]. Several groups have performed the global analysis of the neutrino oscillation results coming from the different experiments [8,61,62]. We have considered the values of neutrino oscillation parameters as listed in Table I, which are reported in the Ref. [8]. We have also ensured that the sum total of light neutrino masses satisfies the limit arising from cosmological data [8] as mentioned in the last row of Table I.

TABLE I. The best-fit value along with 1σ value of neutrino oscillation parameters taken from the global fit [8] of different results coming from various experiments are listed in this table. Here NH and IH refer to the normal hierarchy and inverted hierarchy scenarios, respectively.

	Best-fit value $\pm 1\sigma$	
Neutrino oscillation parameter	NH	IH
Δm^2_{21} [10^{-5}eV^2]	$7.50^{+0.22}_{-0.20}$	$7.50^{+0.22}_{-0.20}$
$\lvert\Delta m^2_{31}\rvert$ [10^{-3}eV^2]	$2.55^{+0.02}_{-0.03}$	$2.45^{+0.02}_{-0.03}$
$\theta_{12}/^\circ$	$34.3^{+1.0}_{-1.0}$	$34.3^{+1.0}_{-1.0}$
$\theta_{13}/^\circ$	$8.53^{+0.13}_{-0.12}$	$8.58^{+0.12}_{-0.14}$
$\theta_{23}/^\circ$	$49.26^{+0.79}_{-0.79}$	$49.46^{+0.60}_{-0.97}$
$\sum m_{\nu_i}$ [eV]	< 0.12	< 0.15

Constraints on the LLE and LQD couplings also arise from nonobservation of neutrinoless double beta decay [63–67]. The existing limits on the lifetime is $\tau > 1.07 \times 10^{26}$ years as quoted by the KamLAND-Zen experiment [68,69], which restricts the λ and λ' couplings to be too large [16].[2]

Some SUSY parameters (e.g., μ, $\tan\beta$) affect the neutrino and Higgs sectors. Therefore, in addition to neutrino data, we have also considered updated data corresponding to the Higgs sector in the form of the SM Higgs mass (m_h) and its coupling strengths. A statistical combination of the updated measurements of the Higgs mass by the ATLAS and CMS Collaborations puts the mass at $125.09 \pm 0.21(\text{stat}) \pm 0.11(\text{syst})$ GeV [70–72]. Considering the theoretical uncertainty within the SUSY framework for the Higgs mass calculation, we use a ± 3 GeV [73] window around the combined best-fit value of m_h. The Higgs boson coupling strength modifiers for each decay channel i are defined as $\kappa_i^2 = \frac{\Gamma_i}{\Gamma_i^{\text{SM}}}$, where Γ_i and Γ_i^{SM} are the BSM and SM contribution to the decay width respectively. Both the ATLAS and CMS Collaborations measure these coupling strength modifiers and present the results with their corresponding uncertainties. The most updated results thus far are quoted in Refs. [33,74]. In this analysis, we only consider the results obtained by the CMS Collaboration [74] and summarize them in Table II.[3] The effective Hiigs-gluon-gluon coupling strength is quite sensitive to the SUSY-breaking scale (M_{SUSY}). However, varying the SUSY breaking scale would require us to vary the trilinear top Yukawa coupling (A_t) and the stop masses as well in addition to $\tan\beta$ and μ in order to ensure the 125 GeV Higgs mass. Therefore, to avoid this complexity and to reduce the

[2]From our analysis we find that the neutrino oscillation data are more constraining.

[3]Note that the ATLAS Collaboration results [33] are very similar and will lead to similar posterior distributions of the input parameters.

TABLE II. The best-fit along with 1σ values of Higgs boson coupling strength modifiers obtained by the CMS Collaboration at $\sqrt{s} = 13$ TeV energy with luminosity $\mathcal{L} = 137$ fb^{-1} [74].

Coupling strength modifiers	Best-fit value $\pm 1\sigma$
κ_z	$0.96^{+0.07}_{-0.07}$
κ_w	$1.11^{+0.14}_{-0.09}$
κ_b	$1.18^{+0.19}_{-0.27}$
κ_τ	$0.94^{+0.12}_{-0.12}$
κ_μ	$0.92^{+0.55}_{-0.87}$
κ_t	$1.01^{+0.11}_{-0.11}$
κ_γ	$1.01^{+0.09}_{-0.14}$

number of free parameters for fast computation, we avoid this scenario as our main focus is on the neutrino sector.

There are different RPC and RPV SUSY contributions to the flavor violating decays like $B \to X_s\gamma$, $B_s \to \mu^+\mu^-$, and $B \to \tau\nu$. So, the limit on the branching ratios of these decays can constrain the parameter space of both RPC and RPV SUSY. There are several RPC contributions to the branching ratio of $B \to X_s\gamma$ decay like gaugino-down type squark, chargino-up type squark, charged Higgs-top quarks, etc. [75,76]. In the RPV SUSY the main contribution is coming from λ' coupling and the contributing coupling products are $\lambda'_{i2j}\lambda'_{i3j}$ and $\lambda'_{ij3}\lambda'_{ij2}$ [16,76,77] corresponding to the $B \to X_s\gamma$ decay branching ratio. Similarly, for $B_s \to \mu^+\mu^-$ decay, the RPC SUSY contributions are Z^0 penguin and box diagrams mediated through charged Higgs boson [78]. The RPV contribution to this branching ratio depends on both the couplings λ and λ' and the related coupling products are $\lambda_{122}\lambda'_{i23}$, $\lambda_{i22}\lambda'_{i32}$, and $\lambda'_{2j2}\lambda'_{2j3}$ [16,77]. There will be a radiative correction to the Higgs boson mass and couplings due to the contributions from charginos, neutralinos, and sfermions, and this change will contribute to the branching ratio of $B \to \tau\nu$ decay. In the RPV SUSY, there will be additional four-fermion interactions due to the exchange of sleptons and squarks, and this will affect the leptonic decays of B meson [16,79]. The relevant coupling product for this decay is $\lambda'_{313}\lambda_{233}$ [16]. As we have considered only λ_{i33} and λ'_{i33} for our analysis, then for all these flavor violating decay, only RPC contribution will be effective. We have taken the value of $B_s \to \mu^+\mu^-$ as $(3.09^{+0.46+0.15}_{-0.43-0.11}) \times 10^{-9}$ which is provided by the LHCb Collaboration [37]. The world average of corresponding to $B \to X_s\gamma$ is given as $(3.32 \pm 0.15) \times 10^{-4}$ in the literature [36]. Similarly, we have also taken into account the branching ratio of $B \to \tau\nu$ as $(1.06 \pm 0.19) \times 10^{-4}$ [36].

IV. CONSTRAINTS OF SPARTICLES FROM DIRECT SEARCHES AT LHC

While fitting the neutrino data, we need to satisfy the current exclusion limit on the sparticle masses coming from the searches using the LHC data. Both the ATLAS and CMS Collaborations have studied a wide range of final states in search of the sparticles. The results coming from these direct searches using Run-I and Run-II data are summarized in Refs. [80,81]. These experimental bounds on sparticle masses are derived with certain simplified assumptions like the presence of only one nonzero RPV coupling, 100% branching ratio to a particular decay mode, etc. In this analysis, as we have considered a model with nonzero values of both the lepton number violating trilinear couplings (λ and λ'), we focus on the corresponding exclusion limits on sparticle masses. In a recent review [17], the authors have discussed in detail about the current exclusion limits on different sparticles with respect to several final state searches for RPV couplings (see Sec. 6 of Ref. [17]). Notably, when the RPV couplings are very small, sparticles are expected to follow RPC SUSY decay modes, and we also include the exclusion limits associated with these RPC decays.

A. Exclusion limits on strong sector

Gluino search: In the RPC framework, the ATLAS and CMS Collaborations have set the most stringent bounds on the masses of gluinos up to ~2.0–2.3 TeV [44,82–88] for different decay modes, with neutralino masses up to 600 GeV. Also, several searches focused on the LQD or LLE coupling using Run-I and Run-II data have been conducted by both the ATLAS [38,89–91] and CMS [87,92] groups where gluino decays indirectly. For λ' coupling the considered decay mode is $\tilde{g} \to q\bar{q}\tilde{\chi}^0_1 \to q\bar{q}(q\bar{q}l/\nu)$, where q, l, and ν refer to light quarks, leptons, and neutrinos, respectively. ATLAS and CMS have excluded gluino masses up to ~2.1–2.2 TeV for bino-type LSP with $m_{\tilde{\chi}^0_1} < 1000$ GeV using LHC Run-II data [87,89,90]. Using the full Run-II dataset, the ATLAS Collaboration has updated the lower bounds on gluino masses up to 2.5 TeV (2.0 TeV) for $\lambda_{121/122}$ ($\lambda_{133/233}$) type LLE scenarios [38].

Squark search: Similar to the gluino searches, both the ATLAS and CMS have conducted squark searches using several final states within the framework of RPC and RPV SUSY models. In RPC MSSM scenarios, these different analyses constrain the lightest stop quark ($\tilde{t}_1$) mass up to 1.0–1.3 TeV [85,86,93–96], the lightest sbottom quark ($\tilde{b}_1$) mass up to 1.15–1.28 TeV [82,86,97], first two generation light squarks mass up to 1.25–1.85 TeV [82–84,86,90,98–101] for a massless neutralino. In the RPV scenarios, the exclusion limit on the $\tilde{t}_1$ mass, from stop NLPS pair production, has reached up to ~820–1020 GeV depending on LLE/LQD couplings [102]. For the production of degenerate first two generations light squark (NLSP), the limits are set at 1.6 TeV [92]. For direct decay of the stop squark, the ATLAS experiment has excluded $\tilde{t}_1$ masses up to 1.9 TeV, 1.8 TeV, and 800 GeV for stop decays to be, $b\mu$, and $b\tau$, respectively, with a 100% branching ratio [42,43].

B. Exclusion limits on electroweak sector

The limits on the electroweak sector are relatively weaker. For winolike lighter chargino ($\tilde{\chi}_1^\pm$) or second lightest neutralino ($\tilde{\chi}_2^0$) and binolike LSP ($\tilde{\chi}_1^0$), the most stringent limits come from $\tilde{\chi}_1^\pm\tilde{\chi}_2^0$ pair production. Depending on the decay modes of NLSP (e.g., slepton mediated, WZ, or Wh mediated), the ATLAS and CMS groups have excluded $m_{\tilde{\chi}_1^\pm}(=m_{\tilde{\chi}_2^0})$ in the range 1–1.2 TeV [40,45,80,81,100,103–109].[4] The CMS Collaboration has also looked for multilepton final state in the context of different RPV leptonic (LLE) and semileptonic (LQD) couplings and excluded wino and Higgsino like LSP in the 300–900 GeV mass range [92]. Considering winolike $\tilde{\chi}_1^\pm\tilde{\chi}_2^0$ pair production and decay of LSP via $\lambda_{121/122}$ ($\lambda_{133/233}$) type LLE couplings the ATLAS group has excluded $\tilde{\chi}_1^\pm$ mass up to 1.6 TeV (1.13) TeV [38]. It may be noted that for a lighter $\tilde{\chi}_1^0$, the limits get reduced drastically, and for our chosen $m_{\tilde{\chi}_1^0}$ (300 GeV), the upper limits on $m_{\tilde{\chi}_1^\pm}$ becomes ~1025 GeV for models with nonzero $\lambda_{133/233}$ couplings. With this same analysis, ATLAS has imposed lower bounds on slepton masses up to 1.2 TeV (860 GeV) for $\lambda_{121/122}$ ($\lambda_{133/233}$) couplings. It may be noted that in RPC SUSY models, where a slepton decays to a lepton and an LSP, the first two generations of sleptons ($\tilde{e}$ and $\tilde{\mu}$) are excluded up to 700 GeV for a massless neutralino ($\tilde{\chi}_1^0$) [44,45], while the limit for the stau is much weaker.

The MSSM Higgs sector, at the tree level, is essentially described by two parameters—pseudoscalar mass (M_A) and $\tan\beta$. The most stringent bound in the M_A—$\tan\beta$ plane comes from the heavy Higgs searches where the neutral heavy Higgs decays via $H/A \to \tau^+\tau^-$ [112,113]. The LHC Run-II data has excluded M_A up to 1.0 (1.5) TeV for $\tan\beta < 8$ (21).

V. DETAILS OF MCMC ANALYSIS SETUP

In this section, we discuss the details of the analysis setup. The analytical calculations for the corresponding trilinear RPV model starting from the Lagrangian are performed through SARAH [114–116], which provides all the files necessary for the required numerical calculations which are subsequently performed by SPheno [117,118]. All the flavor observables mentioned in Sec. III are obtained from FlavorKit [119], which is implemented within the framework of SPheno. SPheno employs two-loop and one-loop calculations for Higgs mass and all other particle masses, respectively. FlavorKit calculates the flavor physics observables up to one loop level. Our primary objective in this analysis is to find out the allowed parameter space in the form of marginal posterior distributions that can fit all the observables while satisfying all constraints detailed in Secs. III and IV. To achieve this, we employ the MCMC method using the publicly available EMCEE code [46]. Our approach involves conducting a likelihood analysis by minimizing the chi-square function defined as

$$\mathcal{L} = \frac{\chi^2}{2} = \frac{1}{2}\sum_{i=1}^{n_{\rm obs}}\left[\frac{X_i^{\rm obs} - X_i^{\rm th}}{\sigma_i}\right]^2, \tag{5.1}$$

where $\mathcal{L}$ represents the negative of log-likelihood, related to the likelihood by $L \propto \exp(-\mathcal{L})$. Here, $X_i^{\rm obs}$ denotes the experimentally observed values of X_i, each with corresponding uncertainties σ_i, and $X_i^{\rm th}$ represents the theoretically calculated value of each observable using our RPV model. In this analysis, we have a total of 16 observables. The number of free parameters is different for different models, which we will discuss in the respective sections, and according to that the degrees of freedom (d.o.f.) will also change. We adopt flat priors for each parameter but draw samples using a Gaussian distribution function. To ensure the comprehensive exploration of the parameter space and to gather sufficient data for drawing 1σ, 2σ, and 3σ contours, we employ 500 walkers ($n_{\rm walker}$) and 400 steps ($n_{\rm step}$) corresponding to each walker. Depending upon the number of cores ($n_{\rm core} \sim 16$–20) we use for the analysis, the number of total generated samples ($n_{\rm walker} \times n_{\rm step} \times n_{\rm core} = 200,000 \times n_{\rm core}$) will be changed. We have also conducted an autocorrelation analysis to ensure that each chain meets the convergence criterion satisfactorily.

In the next section we will focus on estimating the allowed parameter space of different RPV scenarios by calculating the marginalized posterior distribution of various input parameters. The MCMC analysis also searches for the minimum χ^2 ($\chi^2_{\rm min}$) and we calculate the p-value for this χ^2 statistics. The p value is defined as $p = P(\chi^2 \geq \chi^2_{\rm min}|H_0)$ [120] where H_0 is the null hypothesis, typically stating that the model or hypothesis fits the data well. This value can be calculated using the formula $p = \int_{\chi^2_{\rm min}}^{\infty} f(\chi^2, n_d)d\chi^2$, where $f(\chi^2, n_d)$ and n_d refer to the χ^2 statistics and number of degrees of freedom, respectively [120]. A low p value (typically < 0.05) indicates that the model does not fit the observed data well, suggesting the need to reconsider the model or the parameters of the model. On the other hand, a high p value indicates that the model is consistent with the observed data.

VI. RPV MODELS WITH A BINO-LSP

For a generic trilinear RPV model, the number of input parameters is quite large, and scanning the full parameter space is computationally very expensive. As discussed in Sec. II, the dominant contributions to neutrino masses come from the two λ_{i33} ($i = 1, 2$) and three λ'_{i33} ($i = 1, 2, 3$) coupling parameters [16,51–53]. The other relevant parameters in this context are μ, $\tan\beta$, A_d, A_e, and the masses of $\tilde{l}$

[4]For Higgsino pair production this limits reduce to around 200 GeV [110,111] in RPC MSSM.

and $\tilde{q}$. In this work, we sequentially analyze a few simplified models considering the bino-like lightest neutralino ($\tilde{\chi}_1^0$) or top squark ($\tilde{t}_1$) as the LSP. We have analyzed the model with only LQD type couplings (Bino$_{\lambda'}$-model) by varying five input parameters (λ'_{133}, λ'_{233}, λ'_{333}, μ, and $\tan\beta$) and the model with both LLE and LQD couplings (Bino$_{\lambda\lambda'}$-model) by varying seven input (λ_{133}, λ_{233}, λ'_{133}, λ'_{233}, λ'_{333}, μ, and $\tan\beta$) parameters. The soft coupling parameters (A_{i33} or A'_{i33}) are chosen as zero in these three scenarios. Since the soft couplings corresponding to the nonzero λ and λ' couplings do not have any direct contribution to the light neutrino masses and mixings, we chose them to be zero for all these models.[5]

In this section, we probe the above-mentioned two models to fit the neutrino oscillation, Higgs, and flavor data by considering the lightest neutralino ($\tilde{\chi}_1^0$) as the LSP which is bino type. To avoid the current exclusion limits from the LHC, as discussed in Sec. IV, we fix the corresponding soft masses for bino (M_1) at 300 GeV, wino (M_2) at 1200 GeV, gluino (M_3) at 3 TeV, all three generation squark ($m_{\tilde{q}}$) at 3 TeV, all three generation slepton ($m_{\tilde{l}}$) at 2 TeV and M_A at 3 TeV. After some preliminary scans, we have kept the third generation trilinear coupling parameter $A_t = -5.0$ TeV for this scenario so that the SM-like Higgs mass remains around 125 GeV. The ranges of both the varying and fixed values of all input parameters used in our analysis are presented in Table III. We have chosen our ranges exhaustively to ensure that no allowed region is overlooked. For each model, we first obtain the $\chi^2_{\rm min}$, $\chi^2_{\rm min}$/d.o.f., and p value. If the value and the $\chi^2_{\rm min}$/d.o.f. are satisfactory, then we proceed to discuss the allowed parameter space and present the 2D marginalized posterior distribution.

*Model with λ' coupling only (*Bino$_{\lambda'}$*-model):* Since it is quite obvious from Eq. (2.8) that only nonzero λ_{i33} ($i = 1, 2$) cannot be used to fit neutrino oscillation data, first we considered the model with nonzero λ'_{i33} ($i = 1, 2, 3$) couplings keeping the corresponding soft coupling parameters and λ_{i33} couplings zero. The leading order contribution to light neutrino masses arises from quark-squark loops. From Eq. (2.8), one can see that if only LQD type RPV trilinear couplings are nonzero, the mass matrix at the leading order can be approximated as $M_\nu|_{\lambda'} = \frac{3}{8\pi^2\tilde{m}}\lambda'_{i33}\lambda'_{j33}m_b^2$. The degree of freedom for this scenario is 11, as we have 5 free parameters here and 16 observables. We observe that the neutrino oscillation data cannot be fitted with this simplified model. It can explain all the neutrino oscillation observables other than Δm^2_{21}. In this analysis, we have assumed the light neutrino masses align in the normal hierarchy. Consequently, the $\chi^2_{\rm min}$/d.o.f. ~ 100 is on the larger side. Hence, we are not going to discuss this scenario any further.

[5]To check for higher order corrections, we have also considered a Bino$^{AA'}_{\lambda\lambda'}$-model with non-zero soft RPV coupling parameters and presented the results in Appendix B.

TABLE III. Ranges and fixed values of all the input parameters considered in our analysis corresponding to different models. All the parameters are in GeV units except $\tan\beta$, λ, and λ'. Here $i = 1, 2$ ($i = 1, 2, 3$) for λ_{i33} (λ'_{i33}). Also $m_{\tilde{l}}$ refers to all the three generation sleptons (both L type and R type) and $m_{\tilde{q}}$ represents all the generations of squark (both L type and R type) except the third generation L-type squarks which are represented by $m_{\tilde{q}_{3L}}$.

	Value or range of parameters in different models		
	Models with bino LSP		Model with stop LSP
	Only λ'_{i33}	λ_{i33} and λ'_{i33}	λ_{i33} and λ'_{i33}
Parameter	Bino$_{\lambda'}$-model	Bino$_{\lambda\lambda'}$-model	Stop$_{\lambda\lambda'}$-model
$\lvert\lambda_{i33}\rvert$	…	[0–0.001]	[0–0.001]
$\lvert\lambda'_{i33}\rvert$	[0–0.001]	[0–0.001]	[0–0.001]
μ	[800–3000]	[800–3000]	$m_{\tilde{q}_{3L}} + 1000$
$\tan\beta$	[1–60]	[1–60]	[1–60]
$m_{\tilde{q}_{3L}}$	3000	3000	[1000–3000]
M_1	300	300	$m_{\tilde{q}_{3L}} + 1000$
M_2	1200	1200	$m_{\tilde{q}_{3L}} + 1000$
M_3	3000	3000	3000
M_A	3000	3000	3000
A_t	−5000	−5000	4500
$m_{\tilde{l}}$	2000	2000	$m_{\tilde{q}_{3L}} + 500$
$m_{\tilde{q}}$	3000	3000	3000

A. Model with both λ and λ' couplings (Bino$_{\lambda\lambda'}$-model)

We have already discussed that only any one type of coupling cannot explain all the neutrino observables. We need to consider both couplings together [16,54,56,57,121]. The parameter space explored here is mentioned in the Table III. The ranges of 7 input parameters along with other fixed choices for Bino$_{\lambda\lambda'}$-model are tabulated in the fourth column of Table III. Now, we proceed to discuss results corresponding to this model obtained for both the neutrino mass hierarchy.

1. Normal hierarchy scenario

In the normal hierarchy, the third neutrino mass eigenstate (ν_3) is the heaviest and is predominantly τ flavored. The second neutrino mass eigenstate (ν_2) has a slightly lower mass and is an almost equal mixture of all three lepton flavors. The lightest mass eigenstate (ν_1) is primarily e flavored. From our MCMC analysis, the minimum χ^2 value obtained for this scenario is $\chi^2_{\rm min} = 4.14$, leading to $\chi^2_{\rm min}$/d.o.f. $= 0.46$ and p value $= 0.90$. The values of each parameter and observable corresponding to this best-fit point are detailed in Table IV. The masses of the three neutrinos at the best-fit point are $m_{\nu_1} = 2.42 \times 10^{-6}$, $m_{\nu_2} = 8.65 \times 10^{-3}$, and $m_{\nu_3} = 5.04 \times 10^{-2}$ eV, which

TABLE IV. Displayed here are the best-fit and mean values, along with the 1σ uncertainty for all the parameters and best-fit values for the observables in the NH scenario. The last row represents $\chi^2_{\rm min}$, $\chi^2_{\rm min}$/d.o.f. and p value.

Input parameters			Best-fit observable	
Parameter	Best-fit point	Mean value$^{+1\sigma}_{-1\sigma}$	Observable	Best fit
$\lambda_{133} \times 10^{-4}$	1.71	$1.81^{+0.14}_{-0.18}$	Δm^2_{21} [eV^2]	7.49×10^{-5}
			Δm^2_{31} [eV^2]	2.55×10^{-3}
$\lambda_{233} \times 10^{-4}$	2.52	$2.64^{+0.19}_{-0.24}$	θ_{13}	8.53°
			θ_{12}	34.06°
$\lambda'_{133} \times 10^{-5}$	−7.61	$-7.70^{+2.90}_{-0.74}$	θ_{23}	49.30°
			m_h [GeV]	124.88
$\lambda'_{233} \times 10^{-5}$	−7.65	$-8.17^{+0.83}_{-1.99}$	$\mathcal{B}r(B \to X_s\gamma)$	3.15×10^{-4}
			$\mathcal{B}r(B_s \to \mu^+\mu^-)$	3.18×10^{-9}
$\lambda'_{333} \times 10^{-4}$	−1.34	$-1.40^{+0.11}_{-0.08}$	$\mathcal{B}r(B \to \tau\nu)$	1.24×10^{-4}
			κ_z	1.0
μ [GeV]	1996	1820^{+225}_{-300}	κ_w	1.0
			κ_b	1.002
$\tan\beta$	6.68	$6.16^{+2.35}_{-1.36}$	κ_τ	1.002
			κ_μ	1.002
			κ_t	0.999
			κ_γ	1.077
$\chi^2_{\rm min} = 4.14$ $\chi^2_{\rm min}$/d.o.f. $= 0.46$ p value $= 0.90$				

automatically satisfies the limit on the sum of neutrino masses as mentioned in Table I. Only the third neutrino mass gets mass at the leading order as defined in Eq. (2.10). The choice of neutrino mass hierarchy is expected to be reflected in the resulting best-fit values and the 1σ, 2σ, and 3σ ranges of the λ and λ' couplings. In NH of neutrino masses, the third mass eigenstate is considerably heavier compared to the other two states, and hence the best-fit value of λ'_{333} is almost twice that of λ'_{i33} ($i = 1, 2$) with λ'_{233} slightly larger than λ'_{133} as expected. The same trend is visible in best-fit values of λ_{i33} ($i = 1, 2$) as well. These results are reflected in the best-fit values listed in the Table IV. The mean values, along with 2σ allowed regions for each parameter, are also listed in Table IV.

The two-dimensional marginalized posterior distributions corresponding to different parameter planes are shown in Fig. 2 where the dark, lighter, and lightest violet colors represent the 1σ, 2σ, and 3σ regions, respectively. From these 2D contour plots, we have obtained that the allowed regions for μ- $\tan\beta$ parameter space at 95% (68%) confidence level (CL) are 980–2640 (1160–2195) GeV and 2.70–12.70 (3.70–9.60) for μ and $\tan\beta$, respectively. Also the obtained parameter ranges for λ_{133} and λ_{233} parameters at 95% CL are $(1.31\text{–}2.32) \times 10^{-4}$ and $(1.94\text{–}3.23) \times 10^{-4}$ respectively. Similarly the 2σ allowed regions corresponding to *LQD* type RPV couplings are -9.72×10^{-5} to -3.75×10^{-5}, -1.13×10^{-4} to -0.59×10^{-4} and -1.67×10^{-4} to -1.05×10^{-4} for λ'_{133}, λ'_{233}, and λ'_{333} respectively. It is evident from both figures (c) and (d) in Fig. 2 that the λ'_{i33} couplings parameters have more than one allowed region.

The distribution of λ'_{i33} with $i = 1, 2$ exhibits a multimodal posterior, indicating that the model allows multiple solutions for these two parameters. This behavior primarily arises from the dependence on the third neutrino mass eigenstate, as described in Eq. (2.10), which indicates that the mass crucially depends on $\sum_i \lambda^2_{i33}$ where, $i = 1, 2, 3$. Once λ'_{333} picks up a relatively large value owing to normal hierarchy, the other two parameters can combine in more than one way to reproduce the same $\sum_i \lambda^2_{i33}$ factor. The marginalized distribution of each parameter and the correlation of each parameter with every other parameter are shown in Fig. 7 of Appendix A.

2. Inverted hierarchy scenario

In this scenario, the lightest state (ν_3) is dominantly tau flavored. Both ν_1 and ν_2 are heavier and maintain the same hierarchy between them as in the NH scenario. The best-fit point, along with the 1σ uncertainty of each parameter, are shown in the Table V. We have obtained the minimum χ^2 as 4.56 corresponding to 9 d.o.f. which leads to $\chi^2_{\rm min}$/d.o.f. $=$ 0.51 and p value $= 0.87$. The observable values corresponding to the best-fit point are also displayed in the Table V. The neutrino masses at the best-fit point is $m_{\nu_1} = 5.05 \times 10^{-2}$, $m_{\nu_2} = 5.12 \times 10^{-2}$, and $m_{\nu_3} = 3.58 \times 10^{-6}$ eV and the sum of these three neutrino masses are 0.1 which means it satisfies the cosmological limit mentioned in Table I. As in the previous scenario, here also the main contribution to the dominantly tau-flavored neutrino mass eigenstate arises from λ'_{333} coupling with small admixtures

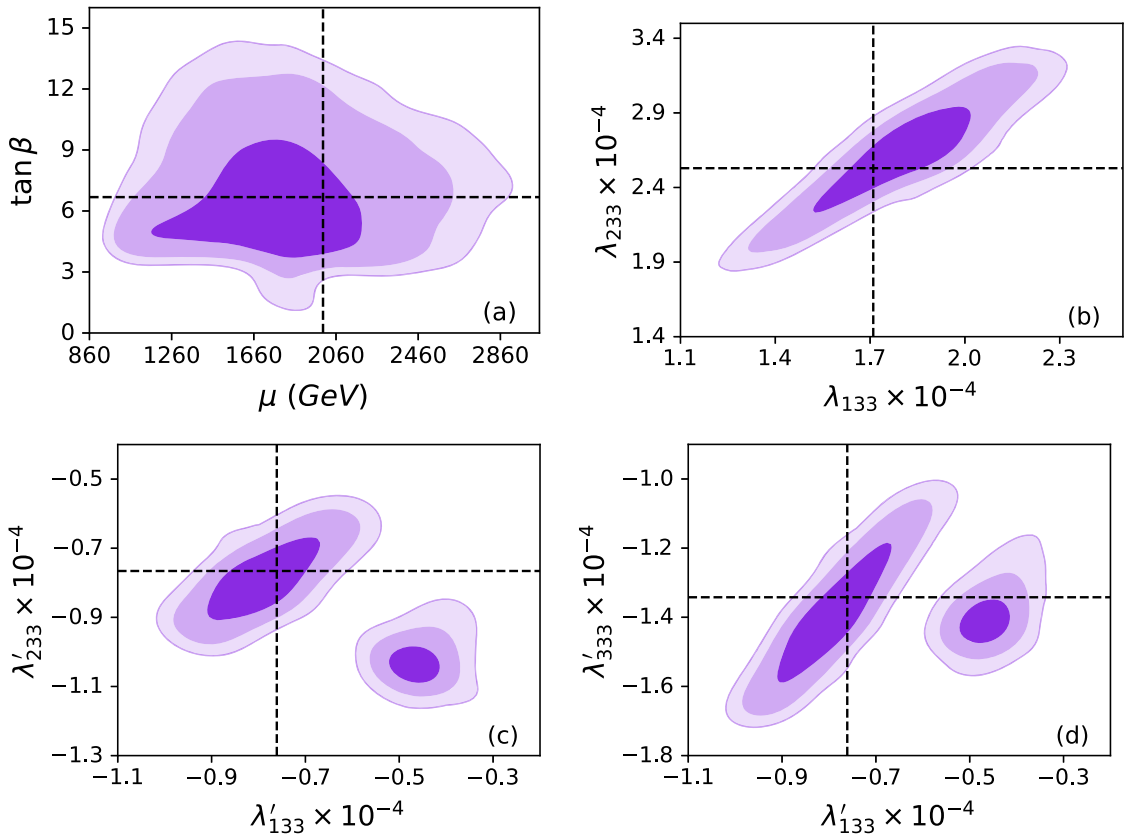


FIG. 2. Marginalized two-dimensional posterior distribution of the parameters in the NH scenario are shown on different planes: (a) $\mu - \tan\beta$ (b) $\lambda_{133} - \lambda_{233}$, (c) $\lambda'_{133} - \lambda'_{233}$, (d) $\lambda'_{133} - \lambda'_{333}$. The dark, lighter, and lightest violet colored regions represent contours at 68%, 95%, and 99% CL. The dashed lines represent the best-fit values of each parameter.

TABLE V. Displayed here are the best-fit and mean values, along with the 1σ uncertainty for all the parameters and best-fit values for the observables in the IH scenario. The last row represents $\chi^2_{\rm min}$, $\chi^2_{\rm min}$/d.o.f. and p value.

Input parameters			Best-fit observable	
Parameter	Best-fit point	Mean value$^{+1\sigma}_{-1\sigma}$	Observable	Best fit
$\lambda_{133} \times 10^{-4}$	2.21	$2.34^{+0.21}_{-0.16}$	Δm^2_{21} [eV^2]	7.50×10^{-5}
			Δm^2_{31} [eV^2]	2.54×10^{-3}
$\lambda_{233} \times 10^{-4}$	4.88	$4.73^{+0.11}_{-0.19}$	θ_{13}	8.54°
			θ_{12}	34.20°
$\lambda'_{133} \times 10^{-4}$	1.29	$1.28^{+0.18}_{-0.08}$	θ_{23}	49.31°
			m_h [GeV]	125.39
$\lambda'_{233} \times 10^{-5}$	−5.92	$-6.43^{+0.54}_{-0.97}$	$\mathcal{B}r(B \to X_s\gamma)$	3.14×10^{-4}
			$\mathcal{B}r(B_s \to \mu^+\mu^-)$	3.17×10^{-9}
$\lambda'_{333} \times 10^{-4}$	−1.25	$-1.22^{+0.60}_{-0.06}$	$\mathcal{B}r(B \to \tau\nu)$	1.25×10^{-4}
			κ_z	1.0
μ [GeV]	1676	1640^{+30}_{-38}	κ_w	1.0
			κ_b	1.001
$\tan\beta$	8.38	$8.67^{+0.53}_{-0.75}$	κ_τ	1.001
			κ_μ	1.001
			κ_t	0.999
			κ_γ	1.098
$\chi^2_{\rm min} = 4.56$ $\chi^2_{\rm min}$/d.o.f. $= 0.51$ p value $= 0.87$				

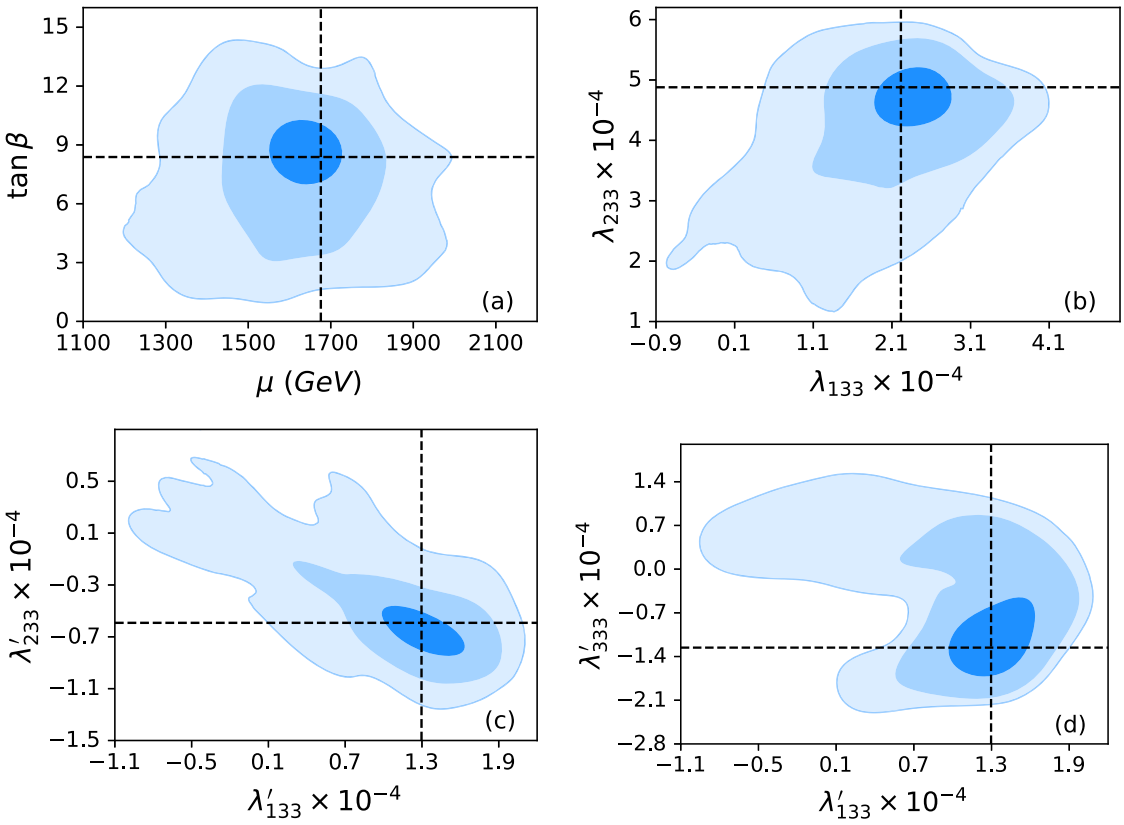


FIG. 3. Marginalized two-dimensional posterior distribution of the parameters in the IH scenario are shown on the different planes: (a) $\mu - \tan\beta$, (b) $\lambda_{133} - \lambda_{233}$, (c) $\lambda'_{133} - \lambda'_{233}$, (d) $\lambda'_{133} - \lambda'_{333}$. The dark, lighter, and lightest blue colored regions represent contours at 68%, 95%, and 99% CL. The dashed lines represent the best-fit values of each parameter.

arising from the other two nonzero λ' couplings. The other two light neutrino mass eigenstates get contribution from both λ_{i33} and λ'_{i33} couplings, where $i = 1, 2$. Small mixing of these states with the dominantly tau-flavored state arises from λ'_{333} coupling as well.

Figure 3 represents the marginalized distributions of the parameter space. Here, the dark and lighter and lightest blue colors refer to the 1σ and 2σ and 3σ regions, respectively, for each figure. The 2σ allowed regions for μ and $\tan\beta$ obtained from the Fig. 3(a) are 1437–1826 GeV and 3.14–12.05, respectively. For *LLE* type RPV couplings the allowed 2σ regions are $(1.24\text{–}3.66) \times 10^{-4}$ and $(3.52\text{–}5.50) \times 10^{-4}$ GeV corresponding to λ_{133} and λ_{233}, respectively. Similarly for λ'_{133}, λ'_{233}, and λ'_{333} couplings the regions are

TABLE VI. Branching ratios of different final sates at the best-fit point coming from single LSP and the LSP pair are shown for the NH scenario. Here l denotes e, μ only.

Final state from single LSP	Final state from LSP pair
	$4\tau + \not{E}_T = 26\%$
$\tau\tau\nu \equiv \tau\tau\nu_e(35.2\%) + \tau\tau\nu_\mu(16.0\%) \rightarrow 51\%$	$1l3\tau + \not{E}_T = 33\%$
$\tau l\nu_\tau \equiv \tau e\nu_\tau(3.6\%) + \tau\mu\nu_\tau(28.5\%) \rightarrow 32\%$	$2l2\tau + \not{E}_T = 10\%$
	$2\tau 2b + \not{E}_T = 16\%$
	$1\tau 1l2b + \not{E}_T = 10\%$
$bb\nu \equiv bb\nu_e(3.1\%) + bb\nu_\mu(3.1\%) + bb\nu_\tau(9.5\%) \rightarrow 16\%$	$4b + \not{E}_T = 2.5\%$
$ltb \equiv etb + \mu tb = 0.5\%$	$1l2\tau 1b1t + \not{E}_T = 1\%$
$\tau tb = 0.7\%$	Others $= 1.5\%$

$(0.27–1.86) \times 10^{-4}$, -1.01×10^{-4} to -0.07×10^{-4}, and -1.97×10^{-4} to -0.87×10^{-4} GeV, respectively. The marginalized distribution of each parameter and the correlation of each parameter with every other parameter are shown in Fig. 8 of Appendix A.

3. Possible collider signals to probe allowed region

It is worth discussing the possible collider signatures of the favored parameter space obtained with a bino LSP. The LSP mass here is chosen to be around 300 GeV, and the wino type lightest chargino ($\tilde{\chi}_1^{\pm}$) or the second lightest neutralino ($\tilde{\chi}_2^0$) becomes the NLSP with a mass around ∼1.25 TeV. We revisit different possible leptonic final states arising from the wino pair production and the sensitivity of the multilepton LHC analyses to probe such scenarios. For the illustration purpose, we present the decay signatures of the LSP at the best-fit point in Table VI for the NH scenario, while the input parameters are already mentioned in Table IV. Note that these results correspond to the best-fit point. Due to the presence of only nonzero λ_{i33} $(i = 1, 2)$ and λ'_{j33} $(j = 1, 2, 3)$ coupling, the LSP decays to $\tau\tau\nu$ and $\tau l\nu_\tau$ final states with 51% and 32% branching ratios, respectively, via LLE couplings and the most dominant decay modes via LQD couplings are $bb\nu_{e/\mu/\tau}$ with a total 16% branching fraction.[6]

In Sec. IV, we have already discussed the limits on wino masses coming from $\tilde{\chi}_1^{\pm}\tilde{\chi}_2^0$ production via $N_l \geq 4l$ and $3l1\tau$ final states, which are sensitive for $\lambda_{121/122}$ and $\lambda_{133/233}$ type LLE couplings. For scenarios with single nonzero λ_{i33} coupling, the LSP pair from the NLSP $(\tilde{\chi}_1^{\pm}, \tilde{\chi}_2^0)$ decays gives rise to $2l2\tau + \not{E}_T$, $1l3\tau + \not{E}_T$ and $4\tau + \not{E}_T$ final states with 25%, 50% and 25% branching ratios respectively and the limits on NLSP masses becomes 500 GeV weaker compared to scenarios with non zero $\lambda_{121/122}$ couplings. For tau enriched final states, the $3l1\tau$ final state search provides a stringent limit on $m_{\tilde{\chi}_1^{\pm}}/m_{\tilde{\chi}_2^0}$ (∼1.025 TeV for a LSP with mass 300 GeV) [38]. From our analysis, for the best-fit point, we observe that the total pure leptonic (including τ) branching fraction is about ∼83%, and this reduction will further weaken the mass limits. It may be noted that for our analysis, the NLSP mass $(m_{\tilde{\chi}_1^{\pm}}/m_{\tilde{\chi}_2^0})$ is ∼1.25 TeV, which is allowed by current LHC data. In a recent analysis [123], the authors have studied the future prospect of electroweakino searches for different choices of LLE couplings from multilepton final states. Furthermore, with b-jet enriched final states, one can probe the scenarios where both LLE and LQD couplings are nonzero, but a dedicated collider analysis in this regard is beyond the scope of this paper. However, using the ATLAS $N_l \geq 4l$ analysis [38], validated in Refs. [123,124], we observe that the lower bounds on $m_{\tilde{\chi}_1^{\pm}}$ reduce to ∼900 GeV when both the LLE and LQD couplings are nonzero, and as a result, the relevant branching ratios get suppressed.

[6]For more detailed discussion on the possible decay channels and LHC signatures with LLE and LQD couplings see Refs. [122,123].

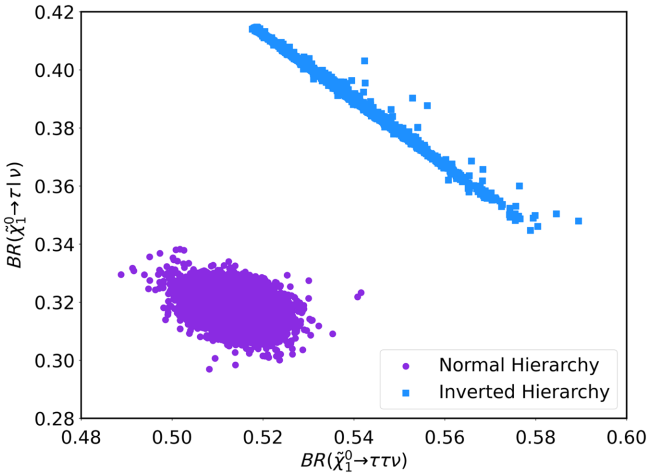


FIG. 4. $\mathcal{B}r(\tilde{\chi}_1^0 \to \tau\tau\nu)$ and $\mathcal{B}r(\tilde{\chi}_1^0 \to \tau l\nu)$ are shown for NH and IH scenarios.

Compared to the NH scenario, the branching ratios of the decays driven by the LLE couplings increase by ∼10% in the IH scenario. This is a direct effect of the resultant hierarchy obtained in the values of the trilinear couplings in our best-fit point. We analyze randomly chosen 10% points within the 3σ allowed region and present the variations in branching ratios for the final states $\tau\tau\nu$ and $\tau l\nu$ in Fig. 4. From the figure, it is evident that the points corresponding to different hierarchy scenarios are clustered in two separate regions. The branching ratios corresponding to IH regions are higher than those for NH points. Consequently, at the LHC, final states with a higher lepton multiplicity are expected in the IH scenario. To illustrate this further, we select two benchmark points from two different scenarios with masses $m_{\tilde{\chi}_1^{\pm}/\tilde{\chi}_2^0} = 1000$ and $m_{\tilde{\chi}_1^0} =$ 300 GeV as shown in Table VII. We evaluate the number of signal events at the hhigh-luminosity LHC (HL-LHC) with $\sqrt{s} = 14$ TeV and $\mathcal{L} = 3000$ fb^{-1} for these benchmark points. For that, we consider the electroweakino pair productions: $pp \to \tilde{\chi}_1^{\pm}\tilde{\chi}_2^0 + \tilde{\chi}_1^{\pm}\tilde{\chi}_1^{\mp}$, where $\tilde{\chi}_1^{\pm} \to \tilde{\chi}_1^0 W^{\pm}$ $(W^{\pm} \to l^{\pm}\nu)$ and $\tilde{\chi}_2^0 \to \tilde{\chi}_1^0 Z$ $(Z \to l^{\pm}l^{\mp})$, with $\tilde{\chi}_1^0$ decaying via both LLE and LQD type couplings. As mentioned earlier, the ATLAS Collaboration has already looked for these electroweakino pair production for with $N_l \geq 4$ final state using Run-II data [38]. Using the same search with $N_l \geq 4$, we estimate that ∼82 and 108 signal events can be obtained at the HL-LHC for the NH and IH scenarios, respectively, assuming that object reconstruction efficiencies and other detector-related factors remain unchanged. The estimated signal yields indicate that there is ∼30%

TABLE VII. The input parameters and the branching ratio corresponding to $\tau\tau\nu$ and $\tau l\nu$ final states are shown for two benchmark points corresponding to two hierarchies are displayed. Here l denotes e, μ only. BP_{NH} and BP_{IH} refers to the benchmark points for normal and inverted hierarchy, respectively.

	Input parameters							Branching ratio	
Bench mark points	λ_{133} $\times 10^{-4}$	λ_{233} $\times 10^{-4}$	λ'_{133} $\times 10^{-4}$	λ'_{233} $\times 10^{-4}$	λ'_{333} $\times 10^{-4}$	μ (GeV)	$\tan\beta$	$\tau\tau\nu$	$\tau l\nu$
BP_{NH}	1.96	2.46	−0.50	−0.98	−1.42	1824.61	6.36	0.524	0.306
BP_{IH}	2.32	4.97	1.35	−0.63	−1.23	1630.16	8.12	0.521	0.414

Masses for both benchmark points	Signal yield at $\sqrt{s} = 14$ TeV and $\mathcal{L} = 3000$ fb^{-1}	
$m_{\tilde{\chi}_1^\pm/\tilde{\chi}_2^0} = 1000$ GeV,	BP_{NH}	BP_{IH}
$m_{\tilde{\chi}_1^0} = 300$ GeV	82	108

enhancement for the IH scenario as compared to the NH scenario. As a result, a careful measurement of the final state events in the above-mentioned leptonic channels can provide an alternate probe of neutrino mass hierarchy at the LHC.

VII. RPV MODEL WITH A STOP LSP (Stop$_{\lambda\lambda'}$-MODEL)

In this section, we analyze the Stop$_{\lambda\lambda'}$-model where the lighter top squark or stop ($\tilde{t}_1$) is the LSP. The mixing effect of the weak eigenstates of the stop in the stop mass matrix is expected to be large due to the presence of the top mass in the off-diagonal term $m_t(A_t - \mu/\tan\beta)$. Thus, the lighter stop mass ($m_{\tilde{t}_1}$) may become much smaller than all other squarks and sparticles.[7] This model-independent large mixing feature could give rise to a theoretically well-motivated stop LSP scenario, as well as a stop NLSP scenario.[8]

For the MCMC analysis, the parameters are varied or fixed as mentioned in the last column of Table III. We vary the masses of third generation left-handed squarks in the range 1–3 TeV, and to obtain the $\tilde{t}_1$ as the LSP, we choose bino, wino, Higgsino masses as $M_1 = M_2 = \mu = m_{\tilde{q}3L} +$ 1000 GeV, all three generation slepton masses as $m_{\tilde{l}} = m_{\tilde{q}_3 L} + 500$ GeV and all other squarks, gluino (M_3) masses and Higgs mass parameter (M_A) fixed at 3 TeV. To achieve a Higgs mass around 125 GeV, we fix A_t at 4.5 TeV. For the Stop$_{\lambda\lambda'}$-model, we only focus on the normal hierarchy scenario with seven free parameters. The best-fit point and the 1σ uncertainty of each parameter, along with the observables values at the best-fit point, are shown in Table VIII. We found that the MCMC analysis leads to χ^2_{min} as 2.93, and the p value becomes 0.96. This scenario provides a better fit to the observable $\mathcal{B}r(B \to X_s\gamma)$ owing to the favored top and bottom squark masses obtained here and thus improves the overall fit quality. The values and hierarchies of the λ_{i33} and λ'_{i33} follow a similar pattern with the NH scenario of the Bino$_{\lambda\lambda'}$-model as discussed in Sec. VI A, but the allowed parameter space is more constrained for this model. The corner plot for this stop-LSP model is shown in Fig. 10 (see Appendix C). Now, we proceed to analyze the characteristics of stop-LSP scenarios in the context of LHC.

A. Possible collider signatures at the LHC and impacts of Run-II data

In general, to satisfy the neutrino oscillation data, the RPV couplings are required to be small. In spite of these tiny couplings, $\tilde{t}_1$ decays via RPV modes to a bottom quark and a charged lepton with 100% branching ratio in the stop-LSP model [132–138]. Hence the final states from stop pair production will consist of an opposite sign dilepton pair along with two hard b-tagged jets ($pp \to \tilde{t}_1\tilde{t}_1^* \to (b\ell^+)(\bar{b}\ell^-)$, where ℓ denotes e, μ, τ). The ATLAS Collaboration has recently conducted a search for stop pair production using the 13 TeV full Run-II dataset and obtained lower limits on $m_{\tilde{t}_1}$ for different choices of branching ratios of three leptonic decay modes [43]. It is important to note that the relative branching ratios among the three leptonic decay modes depend on the choices of the hierarchies of LQD couplings and thus can be useful to discriminate the neutrino mass hierarchy in case the LHC experiment observes any $2b2\ell$ signal. Additionally, we aim to adjudge the effect of the latest LHC limits [43] on the allowed mass ranges of $\tilde{t}_1$, which also satisfy the neutrino oscillation results. As mentioned earlier, the most relevant constraints on the allowed parameter space come from the light stop pair ($\tilde{t}_1\tilde{t}_1^*$) production, and the limits depend on the relative

[7]It may be noted that the renormalization group running from the GUT scale to the weak scale may also suppress the stop mass [13].

[8]Several phenomenological groups have analyzed light stop scenarios in the context of both RPC and RPV models [125–138].

TABLE VIII. The best-fit and mean values with the 1σ uncertainty for the seven free parameters are shown for stop-LSP model in the NH scenario. Last two columns represent best-fit values of the observables. The last row represents $\chi^2_{\rm min}$, $\chi^2_{\rm min}$/d.o.f. and p value.

Input parameters			Best-fit observable	
Parameter	Best-fit point	Mean value$^{+1\sigma}_{-1\sigma}$	Observable	Best-fit
$\lambda_{133} \times 10^{-4}$	1.56	$1.64^{+0.10}_{-0.10}$	Δm^2_{21} [eV^2]	7.50×10^{-5}
			Δm^2_{31} [eV^2]	2.55×10^{-3}
$\lambda_{233} \times 10^{-4}$	2.29	$2.39^{+0.11}_{-0.11}$	θ_{13}	8.52°
			θ_{12}	34.30°
$\lambda'_{133} \times 10^{-5}$	−5.55	$5.56^{+0.24}_{-0.35}$	θ_{23}	49.06°
			m_h [GeV]	125.39
$\lambda'_{233} \times 10^{-5}$	−5.54	$-6.43^{+0.54}_{-0.97}$	$\mathcal{B}r(B \to X_s\gamma)$	3.30×10^{-4}
			$\mathcal{B}r(B_s \to \mu^+\mu^-)$	3.17×10^{-9}
$\lambda'_{333} \times 10^{-4}$	−0.98	$-1.01^{+0.42}_{-0.51}$	$\mathcal{B}r(B \to \tau\nu)$	1.24×10^{-4}
			κ_z	1.0
$\tilde{m}_{q_{3L}}$ [GeV]	1499	1505^{+20}_{-19}	κ_w	1.0
			κ_b	1.001
$\tan\beta$	7.03	$6.08^{+0.53}_{-0.59}$	κ_τ	1.001
			κ_μ	1.001
			κ_t	0.999
			κ_γ	1.098
$\chi^2_{\rm min} = 2.93$ $\chi^2_{\rm min}$/d.o.f. $= 2.93/9 = 0.32$ p value $= 0.96$				

branching ratios among $\tilde{t}_1 \to be, b\mu$, and $b\tau$, which crucially depends on the hierarchies of λ'_{i33} couplings. As mentioned, even with tiny λ'_{i33} couplings, $\tilde{t}_1$ decays to $b\ell(\ell = e,\ \mu,$ and $\tau)$ with 100% branching fractions instead of RPC decays and indirect decays via LLE couplings. It is expected that the branching ratios of the decay modes $\tilde{t}_1 \to b\ell$ will depend on the corresponding λ'_{i33} coupling, which is reflected in Fig. 5.

Here we choose the points[9] with $\chi^2 \le \chi^2_{\rm min} + 11.83$, which corresponds to the allowed χ^2 value for 2D parameter space at the 3σ level [120]. For illustration purpose we present the $\mathcal{B}r(\tilde{t}_1 \to be)$ as a function of λ'_{133} and also show the $\mathcal{B}r(\tilde{t}_1 \to b\tau)$ through the color palette in Fig. 5. $\mathcal{B}r(\tilde{t}_1 \to be)$ gradually increases with higher values λ'_{133} and reaches up to ∼85%, while $\mathcal{B}r(\tilde{t}_1 \to b\tau)$ decreases as $\mathcal{B}r(\tilde{t}_1 \to be + b\mu + b\tau)$ is always unity. The dense red region corresponds to the adjacent region of our best-fit point (with $m_{\tilde{t}_1} = 1470$ GeV), where $\mathcal{B}r(\tilde{t}_1 \to be/b\mu) \sim 0.2$ and $\mathcal{B}r(\tilde{t}_1 \to b\tau) \sim 0.6$. For our best fit point, large $b\tau$ branching arises due to the fact that the λ'_{333} coupling is larger than $\lambda'_{133/233}$ by a factor of 2 (see Table VIII). The LHC sensitivity reduces with the increase of $b\tau$ branching ratio. For example, the lower limit on $m_{\tilde{t}_1}$ reduces from 1900 to 800 GeV in scenarios with a 100% branching ratio to be compared to those with a 100% branching ratio to $b\tau$ [43]. We observe that the branching ratio for the $b\tau$ mode can vary from 0 to 100% in our MCMC-allowed parameter region.

In Fig. 6, we illustrate the impact of existing exclusion limits on $m_{\tilde{t}_1}$ on our allowed parameter space. For this purpose, we have used results obtained by the ATLAS Collaboration [43] and present them in the $\mathcal{B}r(\tilde{t}_1 \to be)$ vs $\mathcal{B}r(\tilde{t}_1 \to b\tau)$ plane. The various colored lines represent the highest limits on $m_{\tilde{t}_1}$ at a 95% CL for a specific point on the branching ratio plane while the total leptonic $(\tilde{t}_1 \to be + b\mu + b\tau)$ branching ratio is assumed to be unity. We use a similar color convention for the representation of the $m_{\tilde{t}_1}$ of 3σ allowed points through the color

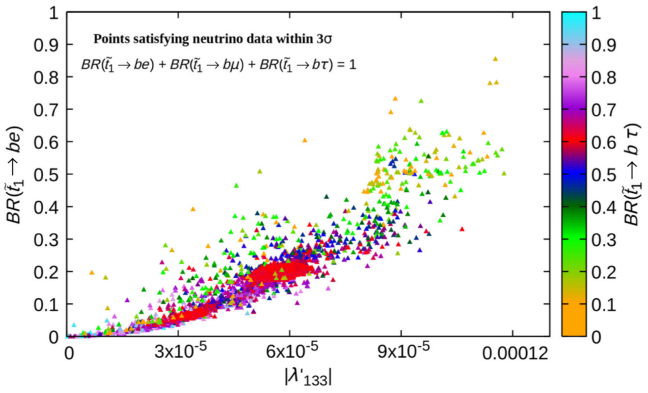


FIG. 5. $\mathcal{B}r(\tilde{t}_1 \to be)$ as a function of $|\lambda'_{133}|$. The $\mathcal{B}r(\tilde{t}_1 \to b\tau)$ branching ratio is also represented by the color palette.

[9]From our final dataset, we have randomly chosen a small fraction (∼6%) of the points to present the results in Figs. 5 and 6.

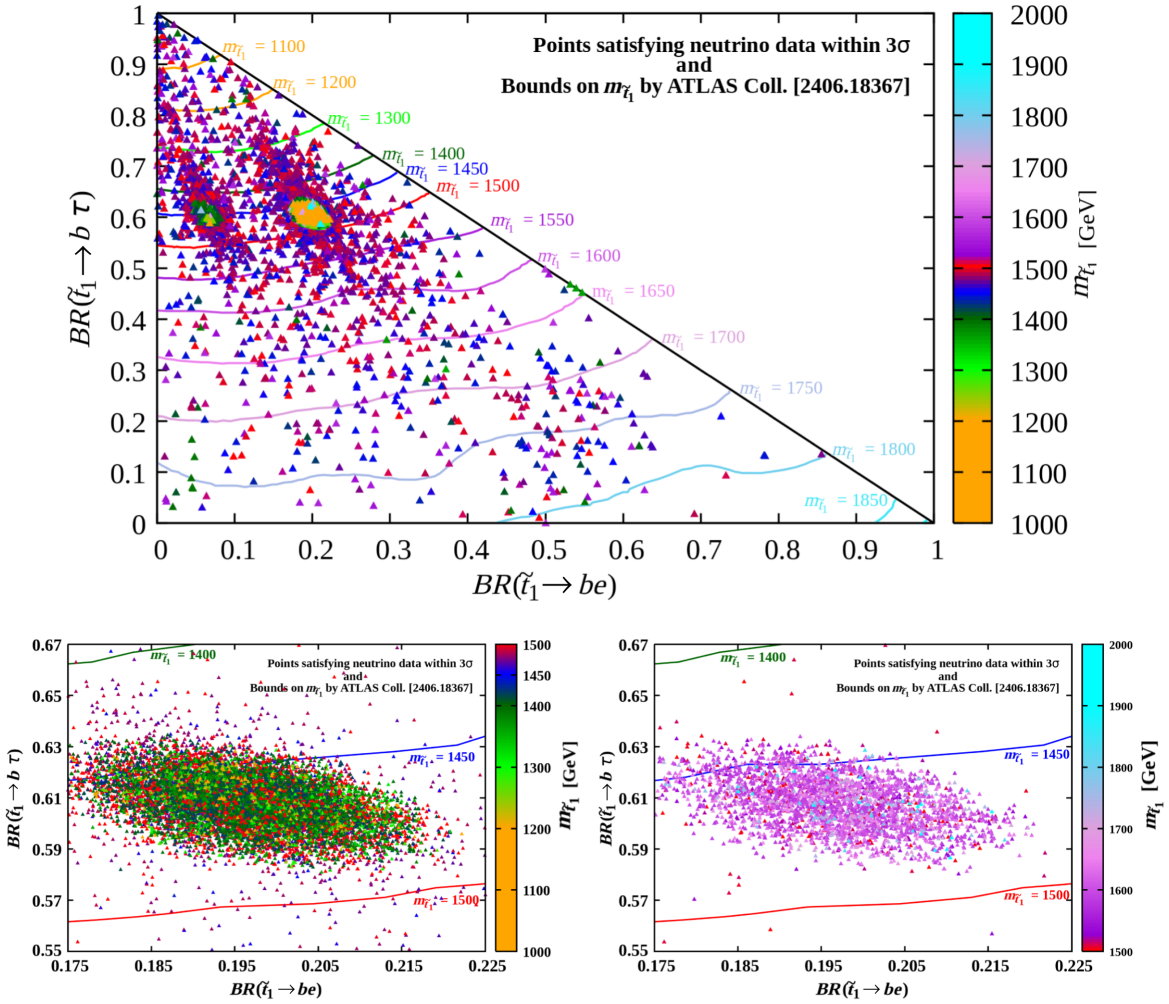


FIG. 6. The interplay of LHC bounds [43] on $m_{\tilde{t}_1}$ as a function of the $\tilde{t}_1$ branching ratios shown, where total $\mathcal{B}r(\tilde{t}_1 \to be + b\mu + b\tau)$ is unity. The different colored lines represent the highest $m_{\tilde{t}_1}$ excluded by the ATLAS Collaboration at 95% C.L. subjected to choice of branching ratio [43]. The points allowed from the MCMC analysis at the 3σ level are shown in the top panel, and the variation of $m_{\tilde{t}_1}$ of these points is illustrated by the color palette with a similar color convention as the limit contours. Thus, any parameter space point with a particular color, which lies below (above) the similar colored exclusion contour, is excluded (allowed) by the LHC Run-II data. Enlarged distribution around the best-fit region presented with $m_{\tilde{t}_1} < 1500$ GeV in the bottom left panel and $m_{\tilde{t}_1} \geq 1500$ GeV in the bottom right panel.

palette. For example, the scattered blue and red points correspond to the parameter space where $m_{\tilde{t}_1}$ is around 1450 and 1500 GeV, respectively, and the LHC data excludes those points with $\mathcal{B}r(\tilde{t}_1 \to b\tau)$ is $\lesssim 0.6$. Parameter space within the mass range $1350 < m_{\tilde{t}_1} < 1400$ GeV (dark green points) are still beyond the reach of current ATLAS analysis where $\mathcal{B}r(\tilde{t}_1 \to b\tau) > 0.7$. The most densely populated region around the best-fit point, with $\mathcal{B}r(\tilde{t}_1 \to be) \sim 0.2$ and $\mathcal{B}r(\tilde{t}_1 \to b\tau) \sim 0.6$, includes parameters space in the stop mass range of $1 < m_{\tilde{t}_1} < 2$ TeV. However, this feature is not clearly visible due to the overlap. Therefore, we zoom in on this region for better illustration purposes and present the results for two mass ranges $m_{\tilde{t}_1} < 1500$ GeV (bottom left panel) and $m_{\tilde{t}_1} \geq 1500$ GeV (bottom right panel) in the Fig. 6. These zoomed plots show that parameter space with light stop mass up to 1350 GeV is excluded while points with $m_{\tilde{t}_1} > 1600$ GeV escape the limits. Note that while generating these plots, we have sampled the allowed region around the best-fit point more extensively, which explains the sparseness of the points in other regions. The key features of these plots are as follows:

(i) All the yellow points ($1000 < m_{\tilde{t}_1} < 1200$ GeV) and the light green points ($m_{\tilde{t}_1} < 1350$ GeV) lie

below the corresponding exclusion line. Even a branching ratio value of $\mathcal{B}r(\tilde{t}_1 \to be + b\mu) \sim 0.4$ is sufficient to exclude these points.

(ii) All dark or light cyan and magenta points correspond to $m_{\tilde{t}_1} > 1600$ GeV and $\mathcal{B}r(\tilde{t}_1 \to b\tau) \sim 0.6$, and these are allowed by the current LHC data.

(iii) The dark green, blue, and red points, corresponding to stop masses around 1400, 1450, and 1500 GeV, respectively, are excluded at 95% CL if the branching ratio of $b\tau$ mode is $< 50\%$. To be precise, a $b\tau$ branching ratio of 72%, 70%, and 65% for these three masses makes the parameter space allowed by the current LHC data. These allowed parameter regions are worth exploring in the context of the future HL-LHC experiment.[10]

VIII. CONCLUSION

R-parity violating supersymmetric theories allow us to include lepton and baryon number violating interaction terms in the Lagrangian. This has immense phenomenological implications. In this work, we have explored scenarios with specific lepton number violating interactions in the context of the latest experimental results. Our main objective has been to ascertain the allowed ranges of these unknown RPV couplings and other relevant SUSY parameters so that they can fit the existing neutrino oscillation data precisely. In addition, we have also considered the SM-like Higgs precision data and B-meson decay branching ratios as observables since their prediction may also be affected while fitting neutrino oscillation data. While performing the analysis, we ensured that the whole parameter space considered in this study also respected the existing collider constraints. We have considered two different scenarios characterized by the choice of the LSP, namely, bino and stop. The analysis has been performed with the help of an MCMC algorithm that not only identifies the best-fit point but can also be used to generate the allowed regions of the model parameter space through likelihood estimation.

We have presented our results in the form of multiple two-dimensional marginalized posterior distributions in different parameter planes, where different confidence level contours are clearly shown. Different trilinear RPV scenarios in the context of neutrino oscillation have been explored before, but this is the first attempt that goes beyond just choosing some benchmark points. What makes our results robust and unique is the fact that we not only provide the whole allowed region, but our results also provide the likelihood of different parts of that allowed region. That gives us an idea of which regions are likely to be probed in the near future. In addition to that, limits on trilinear couplings mostly exist in the literature in product forms, which allows one of the couplings in the product to be somewhat unrestricted compared to the other. Our results put robust constraints on the trilinear couplings individually. Furthermore, any future study on these models must adhere to these constrained parameter spaces presented in this article. Our study indicates that the trilinear couplings λ_{i33} ($i = 1, 2$) and λ'_{j33} ($j = 1, 2, 3$) are all confined to the 10^{-4}–10^{-5} range, whereas, $\tan\beta$ is restricted to values lower than 15. After identifying the allowed regions, we proceeded to discuss what sort of collider signal one can expect for the two different LSP scenarios and comment on their search status in light of the existing collider results. We have observed that the allowed regions obtained from our analysis for the bino-LSP scenarios are mostly allowed by the LHC electroweakino searches while the stop pair production searches partially exclude the parameter space obtained for the stop-LSP scenario. The relevant decay branching ratios of the LSPs for these direct searches reflect the choice of hierarchy and the abundance of the corresponding final state events can be an indirect probe of the neutrino mass hierarchy.

[10]Note that we have not explored the IH scenario with stop LSP. One can expect a comparatively smaller branching ratio of the stop LSP in the $b\tau$ channel in this scenario, leading to more stringent constraints.

ACKNOWLEDGMENTS

A. C. and S. M. acknowledge the Anusandhan National Research Foundation, India, for supporting this work under Core Research Grant No. CRG/2023/008570. S. M. further acknowledges additional support from the Anusandhan National Research Foundation under Core Research Grant No. CRG/2022/003208.

DATA AVAILABILITY

The data are not publicly available. The data are available from the authors upon reasonable request.

APPENDIX A: CORNER PLOT FOR THE MODEL WITH BINO LSP

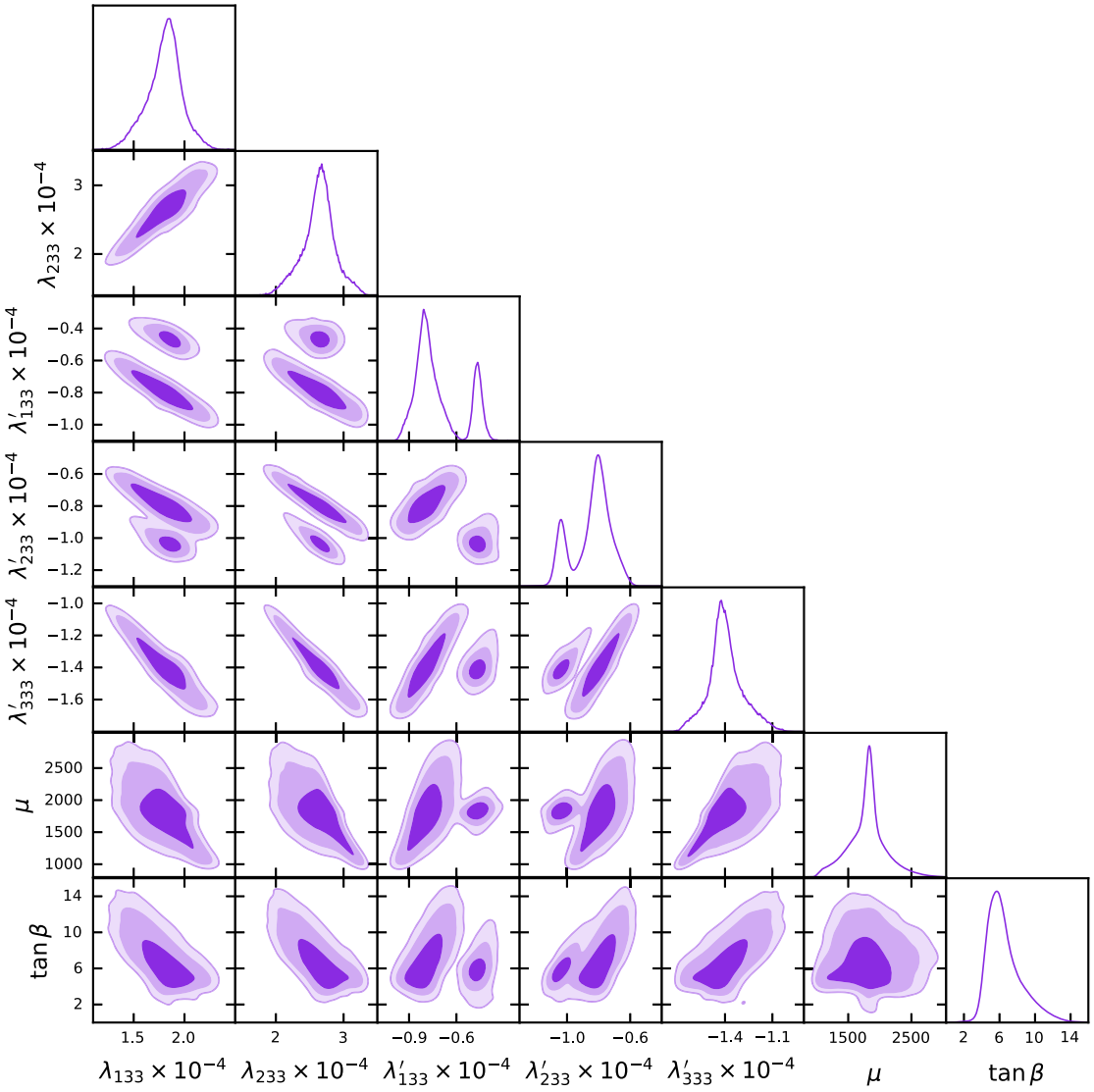


FIG. 7. Corner plot for the input parameters in NH scenario. The diagonal histograms are 1D posterior probability distributions, and the other contour plot show the covariances between parameters. The 1σ, 2σ, and 3σ regions are represented by different shades of violet: dark violet, lighter violet, and lightest violet, respectively.

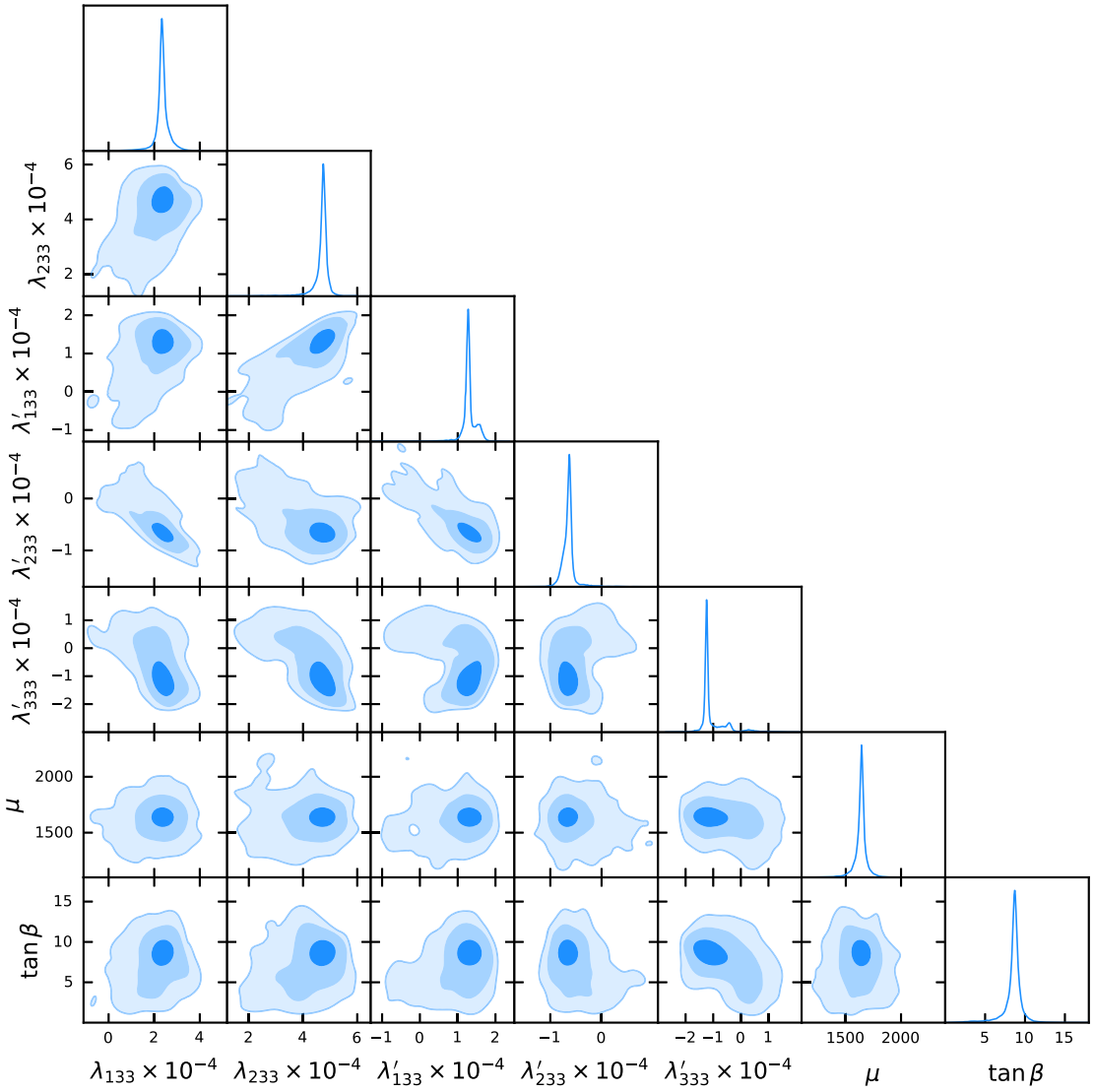


FIG. 8. Corner plot for the input parameters in IH scenario. The diagonal histograms are 1D posterior probability distributions, and the other contour plot show the covariances between parameters. The 1σ, 2σ, and 3σ regions are represented by different shades of blue: dark blue, lighter blue, and lightest blue, respectively.

APPENDIX B: MODEL WITH NONZERO SOFT RPV COUPLING (Bino$^{AA'}_{\lambda\lambda'}$-model)

For completeness, we also have considered a Bino$^{AA'}_{\lambda\lambda'}$-model where the soft coupling parameters corresponding to λ_{i33} and λ'_{i33}, represented as A_{i33} and A'_{i33}, respectively, are also included. These soft couplings introduce five additional parameters in the analysis, hereby increasing the model's complexity. For simplicity, we assume that all A_{i33} have the same value, and similarly, all A'_{i33} have the same value. The range of these two parameters was set to $[-5000, 5000]$ GeV. The rest of the parameters are the same as listed in the third column of Table III. For this analysis, we assume a normal hierarchy in the light neutrino masses. There are 9 free parameters and 16 observables, resulting in 7 degrees of freedom. We have employed similar likelihood based MCMC analysis for Bino$^{AA'}_{\lambda\lambda'}$-model with NH scenario and obtain minimum χ^2 as 4.13 ($\chi^2_{\rm min}$/d.o.f. $= 0.59$), which is similar to the Bino$_{\lambda\lambda'}$-model as discussed in the Sec. VI A 1. This is quite expected since the A and A' couplings do not have any direct contributions to the light neutrino masses and mixings. The best-fit value, mean values, and 1σ uncertainty of the parameters, along with the values of observables at the best-fit point, are listed in Table IX. We have shown the 68%, 95%, and 99% CL contours corresponding to these two parameters in the Fig. 9. From this plot, we can see that A_{i33} and A'_{i33} can have a 2σ region as -2300 to 2600 GeV and -710 to 775 GeV, respectively. Note that the values of A_{i33} and A'_{i33} at the best-fit point are -45 and 13 GeV, respectively, which are very close to the choice ($A_{i33} = A'_{i33} = 0$) we made for other scenarios.

TABLE IX. The best-fit and mean values, along with the 1σ uncertainty for all the parameters and best-fit values for the observables in the NH scenario of the model with nonzero soft RPV couplings are shown here. The last row represents $\chi^2_{\rm min}$, corresponding $\chi^2_{\rm min}$/d.o.f. and p value.

Input parameters			Best-fit observable	
Parameter	Best-fit point	Mean value$^{+1\sigma}_{-1\sigma}$	Observable	Best-fit
$\lambda_{133} \times 10^{-4}$	1.82	$1.82^{+0.44}_{-1.03}$	Δm^2_{21} [eV^2]	7.49×10^{-5}
			Δm^2_{31} [eV^2]	2.55×10^{-3}
$\lambda_{233} \times 10^{-4}$	2.69	$2.65^{+0.52}_{-0.98}$	θ_{13}	8.53°
			θ_{12}	34.06°
$\lambda'_{133} \times 10^{-4}$	−0.45	$-0.77^{+1.25}_{-0.51}$	θ_{23}	49.30°
			m_h [GeV]	124.88
$\lambda'_{233} \times 10^{-4}$	−1.04	$-0.81^{+1.45}_{-0.38}$	$\mathcal{B}r(B \to X_s\gamma)$	3.15×10^{-4}
			$\mathcal{B}r(B_s \to \mu^+\mu^-)$	3.18×10^{-9}
$\lambda'_{333} \times 10^{-4}$	−1.41	$-1.41^{+0.92}_{-0.25}$	$\mathcal{B}r(B \to \tau\nu)$	1.24×10^{-4}
			κ_z	1.0
μ [GeV]	1827	1851^{+193}_{-226}	κ_w	1.0
			κ_b	1.002
$\tan\beta$	5.94	$5.96^{+3.22}_{-2.66}$	κ_τ	1.002
			κ_μ	1.002
A_{i33}	−45	105^{+1183}_{-1198}	κ_t	0.999
A'_{i33}	13	-35^{+445}_{-463}	κ_γ	1.077
$\chi^2_{\rm min} = 4.13$ $\chi^2_{\rm min}$/d.o.f. $= 0.59$ p value $= 0.75$				

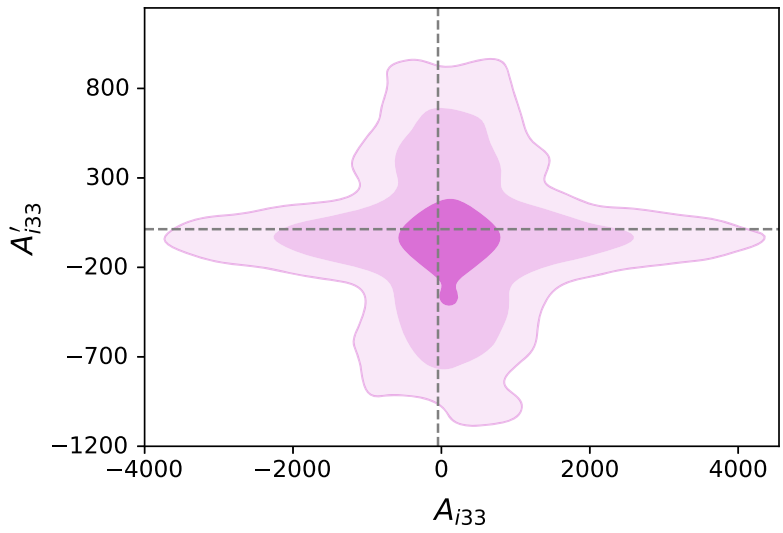


FIG. 9. The posterior distribution of A_{i33} and A'_{i33} is shown here. The dark, lighter, and lightest magenta colors represent contours at 68%, 95%, and 99% CL. Here, we have considered that two A_{i33} have the same value and similarly, all the A'_{i33} have the same value. Light neutrino masses follow NH.

APPENDIX C: CORNER PLOT FOR THE MODEL WITH STOP LSP

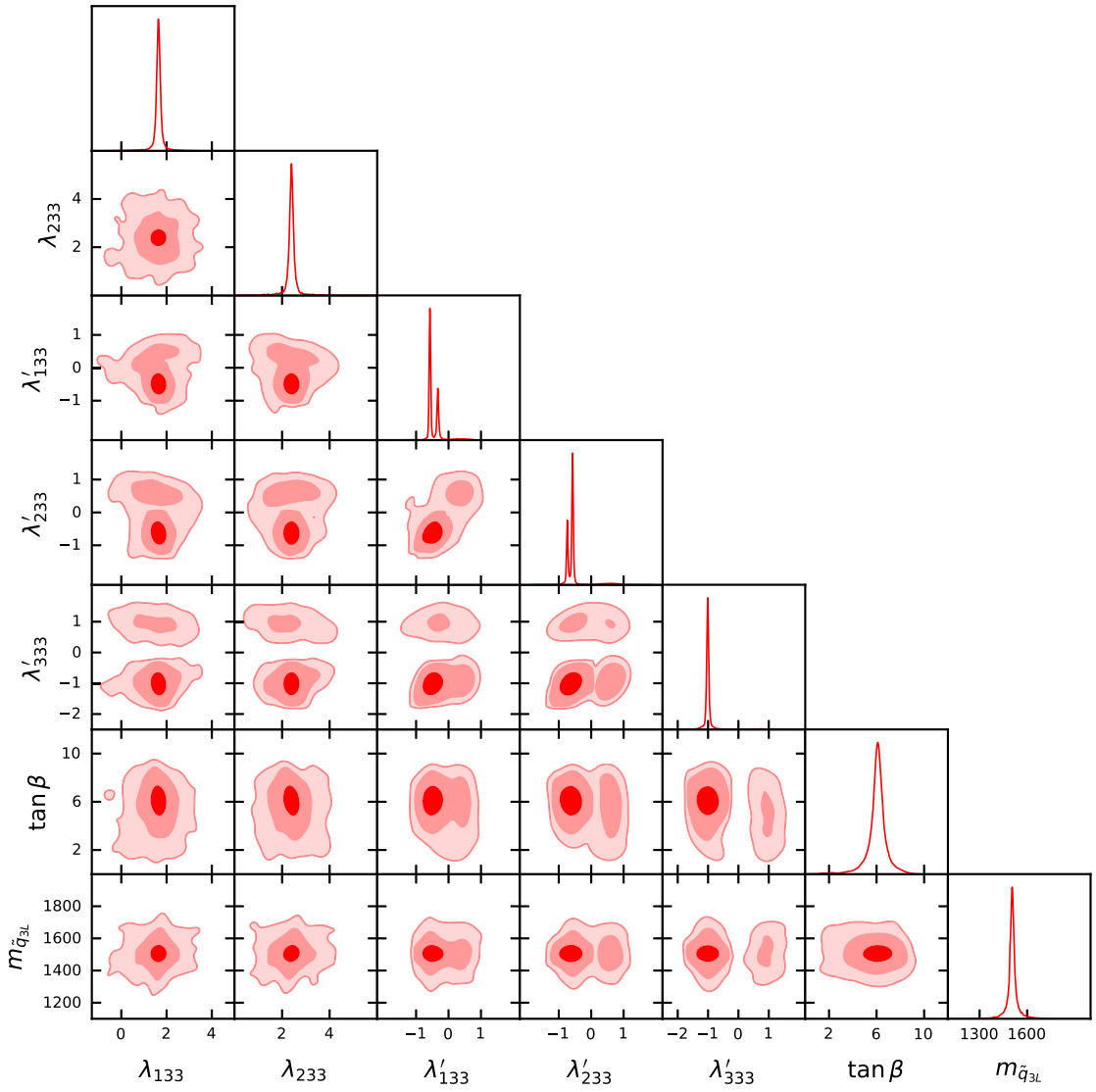


FIG. 10. Corner plot for the input parameters in the NH scenario for the model with stop LSP. The diagonal histograms are 1D posterior probability distributions, and the other contour plot show the covariances between parameters. The 1σ, 2σ, and 3σ regions are represented by different shades of red: dark red, lighter red, and lightest red, respectively.

[1] G. Bellini *et al.* (Borexino Collaboration), Final results of Borexino phase-I on low energy solar neutrino spectroscopy, Phys. Rev. D **89**, 112007 (2014).

[2] A. Gando *et al.* (KamLAND Collaboration), Reactor on-off antineutrino measurement with KamLAND, Phys. Rev. D **88**, 033001 (2013).

[3] G. Bak *et al.* (RENO Collaboration), Measurement of reactor antineutrino oscillation amplitude and frequency at RENO, Phys. Rev. Lett. **121**, 201801 (2018).
[4] D. Adey *et al.* (Daya Bay Collaboration), Measurement of the electron antineutrino oscillation with 1958 days of operation at Daya Bay, Phys. Rev. Lett. **121**, 241805 (2018).
[5] M. Jiang *et al.* (Super-Kamiokande Collaboration), Atmospheric neutrino oscillation analysis with improved event reconstruction in Super-Kamiokande IV, Prog. Theor. Exp. Phys. **2019**, 053F01 (2019).
[6] K. Abe *et al.* (T2K Collaboration), Search for *CP* violation in neutrino and antineutrino oscillations by the T2K experiment with 2.2×10^{21} protons on target, Phys. Rev. Lett. **121**, 171802 (2018).
[7] M. A. Acero *et al.* (NOvA Collaboration), First measurement of neutrino oscillation parameters using neutrinos and antineutrinos by NOvA, Phys. Rev. Lett. **123**, 151803 (2019).
[8] P. F. de Salas, D. V. Forero, S. Gariazzo, P. Martínez-Miravé, O. Mena, C. A. Ternes, M. Tórtola, and J. W. F. Valle, 2020 global reassessment of the neutrino oscillation picture, J. High Energy Phys. 02 (2021) 071.
[9] S. L. Glashow, Partial-symmetries of weak interactions, Nucl. Phys. **22**, 579 (1961).
[10] S. Weinberg, A model of leptons, Phys. Rev. Lett. **19**, 1264 (1967).
[11] A. Salam, Weak and electromagnetic interactions, Conf. Proc. C **680519**, 367 (1968).
[12] M. Gell-Mann, A schematic model of baryons and mesons, Phys. Lett. **8**, 214 (1964).
[13] S. P. Martin, A supersymmetry primer, Adv. Ser. Dir. High Energy Phys. **18**, 1 (1998).
[14] M. Drees, R. Godbole, and P. Roy, *Theory and Phenomenology of Sparticles: An Account of Four-Dimensional N=1 Supersymmetry in High Energy Physics* (World Scientic Publishing Co., 2004).
[15] H. Baer and X. Tata, *Weak Scale Supersymmetry: From Superfields to Scattering Events* (Cambridge University Press, Cambridge, England, 2006).
[16] R. Barbier *et al.*, R-parity violating supersymmetry, Phys. Rep. **420**, 1 (2005).
[17] A. Choudhury, A. Mondal, and S. Mondal, Status of R-parity violating SUSY, Eur. Phys. J. Special Topics **233**, 2187 (2024).
[18] B. C. Allanach, A. Dedes, and H. K. Dreiner, R parity violating minimal supergravity model, Phys. Rev. D **69**, 115002 (2004).
[19] Y. Grossman and H. E. Haber, Sneutrino mixing phenomena, Phys. Rev. Lett. **78**, 3438 (1997).
[20] Y. Grossman and S. Rakshit, Neutrino masses in R-parity violating supersymmetric models, Phys. Rev. D **69**, 093002 (2004).
[21] S. Rakshit, Neutrino masses and R-parity violation, Mod. Phys. Lett. A **19**, 2239 (2004).
[22] R. Hempfling, Neutrino masses and mixing angles in SUSY GUT theories with explicit R-parity breaking, Nucl. Phys. **B478**, 3 (1996).
[23] B. C. Allanach, A. Dedes, and H. K. Dreiner, Bounds on R-parity violating couplings at the weak scale and at the GUT scale, Phys. Rev. D **60**, 075014 (1999).
[24] M. Góźdź and W. A. Kamiński, Constraining bilinear *r*-parity violation from neutrino masses, Phys. Rev. D **78**, 075021 (2008).
[25] R. S. Hundi, Constraints from neutrino masses and muon (g-2) in the bilinear R-parity violating supersymmetric model, Phys. Rev. D **83**, 115019 (2011).
[26] M. A. Díaz, M. Rivera, and N. Rojas, On neutrino masses in the MSSM with BRpV, Nucl. Phys. **B887**, 338 (2014).
[27] F. de Campos, O. J. P. Eboli, M. B. Magro, W. Porod, D. Restrepo, S. P. Das, M. Hirsch, and J. W. F. Valle, Probing neutralino properties in minimal supergravity with bilinear R-parity violation, Phys. Rev. D **86**, 075001 (2012).
[28] M. Hirsch, M. A. Diaz, W. Porod, J. C. Romao, and J. W. F. Valle, Neutrino masses and mixings from supersymmetry with bilinear R parity violation: A theory for solar and atmospheric neutrino oscillations, Phys. Rev. D **62**, 113008 (2000).
[29] A. Choudhury, S. Mitra, A. Mondal, and S. Mondal, Bilinear R-parity violating supersymmetry under the light of neutrino oscillation, Higgs and flavor data, J. High Energy Phys. 02 (2024) 004.
[30] S. Roy and B. Mukhopadhyaya, Some implications of a supersymmetric model with R-parity breaking bilinear interactions, Phys. Rev. D **55**, 7020 (1997).
[31] E. Nardi, Renormalization group induced neutrino masses in supersymmetry without R-parity, Phys. Rev. D **55**, 5772 (1997).
[32] B. de Carlos and P. L. White, R-parity violation effects through soft supersymmetry breaking terms and the renormalization group, Phys. Rev. D **54**, 3427 (1996).
[33] ATLAS Collaboration, Combined measurements of Higgs boson production and decay using up to 139 fb^{-1} of proton-proton collision data at $\sqrt{s} = 13$ TeV collected with the ATLAS experiment, Report No. ATLAS-CONF-2021-053, 2021.
[34] CMS Collaboration, CMS analysis physics summary, https://cds.cern.ch/record/2706103/files/HIG-19-005-pas.pdf (2019).
[35] F. Archilli, M. O. Bettler, P. Owen, and K. A. Petridis, Flavour-changing neutral currents making and breaking the standard model, Nature (London) **546**, 221 (2017).
[36] Y. S. Amhis *et al.* (HFLAV Collaboration), Averages of b-hadron, c-hadron, and τ-lepton properties as of 2018, Eur. Phys. J. C **81**, 226 (2021).
[37] R. Aaij *et al.* (LHCb Collaboration), Analysis of neutral *B*-meson decays into two muons, Phys. Rev. Lett. **128**, 041801 (2022).
[38] G. Aad *et al.* (ATLAS Collaboration), Search for supersymmetry in events with four or more charged leptons in 139 fb^{-1} of $\sqrt{s} = 13$ TeV pp collisions with the ATLAS detector, J. High Energy Phys. 07 (2021) 167.
[39] R. K. Barman, B. Bhattacherjee, I. Chakraborty, A. Choudhury, and N. Khan, Electroweakino searches at

the HL-LHC in the baryon number violating MSSM, Phys. Rev. D **103**, 015003 (2021).
[40] G. Aad *et al.* (ATLAS Collaboration), Search for chargino–neutralino pair production in final states with three leptons and missing transverse momentum in $\sqrt{s} = 13$ TeV pp collisions with the ATLAS detector, Eur. Phys. J. C **81**, 1118 (2021).
[41] G. Aad *et al.* (ATLAS Collaboration), Search for direct production of winos and higgsinos in events with two same-charge leptons or three leptons in pp collision data at $\sqrt{s} = 13$ TeV with the ATLAS detector, J. High Energy Phys. 11 (2023) 150.
[42] M. Aaboud *et al.* (ATLAS Collaboration), Search for B-L R-parity-violating top squarks in $\sqrt{s} = 13$ TeV pp collisions with the ATLAS experiment, Phys. Rev. D **97**, 032003 (2018).
[43] G. Aad *et al.* (ATLAS Collaboration), A search for R-parity violating supersymmetric decays of the top squark to a b-jet and a lepton in $\sqrt{s} = 13$ TeV pp collisions with the ATLAS detector, Phys. Rev. D **110**, 092004 (2024).
[44] A. M. Sirunyan *et al.* (CMS Collaboration), Search for supersymmetry in final states with two oppositely charged same-flavor leptons and missing transverse momentum in proton-proton collisions at $\sqrt{s} = 13$ TeV, J. High Energy Phys. 04 (2021) 123.
[45] G. Aad *et al.* (ATLAS Collaboration), Search for electroweak production of charginos and sleptons decaying into final states with two leptons and missing transverse momentum in $\sqrt{s} = 13$ TeV pp collisions using the ATLAS detector, Eur. Phys. J. C **80**, 123 (2020).
[46] D. Foreman-Mackey, D. W. Hogg, D. Lang, and J. Goodman, EMCEE: The MCMC hammer, Publ. Astron. Soc. Pac. **125**, 306 (2013).
[47] H. K. Dreiner, An introduction to explicit R-parity violation, Adv. Ser. Dir. High Energy Phys. **21**, 565 (2010).
[48] T. Banks, Y. Grossman, E. Nardi, and Y. Nir, Supersymmetry without R-parity and without lepton number, Phys. Rev. D **52**, 5319 (1995).
[49] L. J. Hall and M. Suzuki, Explicit R-parity breaking in supersymmetric models, Nucl. Phys. **B231**, 419 (1984).
[50] K. S. Babu and R. N. Mohapatra, Supersymmetry and large transition magnetic moment of the neutrino, Phys. Rev. Lett. **64**, 1705 (1990).
[51] Y. Grossman and H. E. Haber, (S)neutrino properties in R-parity violating supersymmetry. 1. CP conserving phenomena, Phys. Rev. D **59**, 093008 (1999).
[52] A. S. Joshipura and S. K. Vempati, Sneutrino vacuum expectation values and neutrino anomalies through trilinear R-parity violation, Phys. Rev. D **60**, 111303 (1999).
[53] S. Davidson and M. Losada, Basis independent neutrino masses in the R_p violating MSSM, Phys. Rev. D **65**, 075025 (2002).
[54] T. Banks, Y. Grossman, E. Nardi, and Y. Nir, Supersymmetry without r parity and without lepton number, Phys. Rev. D **52**, 5319 (1995).
[55] P. Binetruy, E. Dudas, S. Lavignac, and C. A. Savoy, Quark flavor conserving violations of the lepton number, Phys. Lett. B **422**, 171 (1998).
[56] F. M. Borzumati, Y. Grossman, E. Nardi, and Y. Nir, Neutrino masses and mixing in supersymmetric models without R parity, Phys. Lett. B **384**, 123 (1996).
[57] H. K. Dreiner, D. Köhler, and S. Nangia, A ν approach to analyzing neutrino data in the **R**-parity-violating MSSM, Eur. Phys. J. C **83**, 44 (2023).
[58] A. Donini, M. B. Gavela, P. Hernandez, and S. Rigolin, Neutrino mixing and CP violation, Nucl. Phys. **B574**, 23 (2000).
[59] E. K. Akhmedov, Neutrino physics, in *ICTP Summer School in Particle Physics* (1999), pp. 103–164, arXiv: hep-ph/0001264.
[60] C. Giganti, S. Lavignac, and M. Zito, Neutrino oscillations: The rise of the PMNS paradigm, Prog. Part. Nucl. Phys. **98**, 1 (2018).
[61] I. Esteban, M. C. Gonzalez-Garcia, M. Maltoni, I. Martinez-Soler, and T. Schwetz, Updated fit to three neutrino mixing: Exploring the accelerator-reactor complementarity, J. High Energy Phys. 01 (2017) 087.
[62] I. Esteban, M. C. Gonzalez-Garcia, M. Maltoni, T. Schwetz, and A. Zhou, The fate of hints: Updated global analysis of three-flavor neutrino oscillations, J. High Energy Phys. 09 (2020) 178.
[63] K. S. Babu and R. N. Mohapatra, New vector—scalar contributions to neutrinoless double beta decay and constraints on R-parity violation, Phys. Rev. Lett. **75**, 2276 (1995).
[64] M. Hirsch, H. V. Klapdor-Kleingrothaus, and S. G. Kovalenko, New supersymmetric contributions to neutrinoless double beta decay, Phys. Lett. B **352**, 1 (1995).
[65] M. Hirsch, H. V. Klapdor-Kleingrothaus, and S. G. Kovalenko, Supersymmetry and neutrinoless double beta decay, Phys. Rev. D **53**, 1329 (1996).
[66] B. Allanach, S. Biswas, S. Mondal, and M. Mitra, Explaining a CMS $eejj$ excess with $\mathcal{R}$-parity violating supersymmetry and implications for neutrinoless double beta decay, Phys. Rev. D **91**, 011702 (2015).
[67] B. C. Allanach, S. Biswas, S. Mondal, and M. Mitra, Resonant slepton production yields CMS $eejj$ and $ep_T jj$ excesses, Phys. Rev. D **91**, 015011 (2015).
[68] B. J. P. Jones, The physics of neutrinoless double beta decay: A primer, in *Theoretical Advanced Study Institute in Elementary Particle Physics: The Obscure Universe: Neutrinos and Other Dark Matters* (2021), arXiv: 2108.09364.
[69] A. Gando *et al.* (KamLAND-Zen Collaboration), Search for Majorana neutrinos near the inverted mass hierarchy region with KamLAND-Zen, Phys. Rev. Lett. **117**, 082503 (2016).
[70] S. Chatrchyan *et al.* (CMS Collaboration), Observation of a new boson at a mass of 125 GeV with the CMS experiment at the LHC, Phys. Lett. B **716**, 30 (2012).
[71] G. Aad *et al.* (ATLAS Collaboration), Observation of a new particle in the search for the standard model Higgs boson with the ATLAS detector at the LHC, Phys. Lett. B **716**, 1 (2012).

[72] G. Aad *et al.* (ATLAS and CMS Collaborations), Combined measurement of the Higgs boson mass in pp Collisions at $\sqrt{s} = 7$ and 8 TeV with the ATLAS and CMS experiments, Phys. Rev. Lett. **114**, 191803 (2015).
[73] B. C. Allanach, A. Djouadi, J. L. Kneur, W. Porod, and P. Slavich, Precise determination of the neutral Higgs boson masses in the MSSM, J. High Energy Phys. 09 (2004) 044.
[74] CMS Collaboration, Combined Higgs boson production and decay measurements with up to 137 fb^{-1} of proton-proton collision data at $\sqrt{s} = 13$ TeV, Technical Report No. CMS-PAS-HIG-19-005, CERN, Geneva, 2020.
[75] S. Bertolini and F. Vissani, Supersymmetric predictions for the inclusive $b \to s\gamma$ decay, Z. Phys. C **67**, 513 (1995).
[76] B. de Carlos and P. L. White, R-parity violation and quark flavor violation, Phys. Rev. D **55**, 4222 (1997).
[77] H. K. Dreiner, K. Nickel, and F. Staub, $B^0_{s,d} \to \mu\bar{\mu}$ and $B \to X_s\gamma$ in the R-parity violating MSSM, Phys. Rev. D **88**, 115001 (2013).
[78] K. S. Babu and C. F. Kolda, Higgs mediated $B^0 \to \mu^+\mu^-$ in minimal supersymmetry, Phys. Rev. Lett. **84**, 228 (2000).
[79] S. Baek and Y. G. Kim, Constraints on the R-parity violating couplings from $B^{\pm} \to l^{\pm}\nu$ decays, Phys. Rev. D **60**, 077701 (1999).
[80] ATLAS Collaboration, ATLAS experiment—public results, https://twiki.cern.ch/twiki/bin/view/AtlasPublic/SupersymmetryPublicResults (2023).
[81] CMS Collaboration, CMS experiment—physics results, https://twiki.cern.ch/twiki/bin/view/CMSPublic/PhysicsResultsSUS (2023).
[82] The CMS Collaboration *et al.*, Search for supersymmetry in proton-proton collisions at 13 TeV in final states with jets and missing transverse momentum, J. High Energy Phys. 10 (2019) 244.
[83] G. Aad *et al.* (ATLAS Collaboration), Search for squarks and gluinos in final states with jets and missing transverse momentum using 139 fb^{-1} of $\sqrt{s} = 13$ TeV pp collision data with the ATLAS detector, J. High Energy Phys. 02 (2021) 143.
[84] G. Aad *et al.* (ATLAS Collaboration), Search for squarks and gluinos in final states with one isolated lepton, jets, and missing transverse momentum at $\sqrt{s} = 13$ with the ATLAS detector, Eur. Phys. J. C **81**, 600 (2021).
[85] A. M. Sirunyan *et al.* (CMS Collaboration), Search for top squark production in fully-hadronic final states in proton-proton collisions at $\sqrt{s} = 13$ TeV, Phys. Rev. D **104**, 052001 (2021).
[86] A. M. Sirunyan *et al.* (CMS Collaboration), Searches for physics beyond the standard model with the M_{T2} variable in hadronic final states with and without disappearing tracks in proton-proton collisions at $\sqrt{s} = 13$ TeV, Eur. Phys. J. C **80**, 3 (2020).
[87] A. M. Sirunyan *et al.* (CMS Collaboration), Search for physics beyond the standard model in events with jets and two same-sign or at least three charged leptons in proton-proton collisions at $\sqrt{s} = 13$ TeV, Eur. Phys. J. C **80**, 752 (2020).
[88] A. Tumasyan *et al.* (CMS Collaboration), Search for supersymmetry in final states with a single electron or muon using angular correlations and heavy-object identification in proton-proton collisions at $\sqrt{s} = 13$ TeV, J. High Energy Phys. 09 (2023) 149.
[89] G. Aad *et al.* (ATLAS Collaboration), Search for R-parity-violating supersymmetry in a final state containing leptons and many jets with the ATLAS experiment using $\sqrt{s} =$ 13 TeV proton–proton collision data, Eur. Phys. J. C **81**, 1023 (2021).
[90] G. Aad *et al.* (ATLAS Collaboration), Search for pair production of squarks or gluinos decaying via sleptons or weak bosons in final states with two same-sign or three leptons with the ATLAS detector, J. High Energy Phys. 02 (2024) 107.
[91] M. Aaboud *et al.* (ATLAS Collaboration), Search for supersymmetry in events with four or more leptons in $\sqrt{s} = 13$ TeV pp collisions with ATLAS, Phys. Rev. D **98**, 032009 (2018).
[92] V. Khachatryan *et al.* (CMS Collaboration), Searches for R-parity-violating supersymmetry in pp collisions at $\sqrt{s} = 8$ TeV in final states with 0-4 leptons, Phys. Rev. D **94**, 112009 (2016).
[93] A. M. Sirunyan *et al.* (CMS Collaboration), Search for direct top squark pair production in events with one lepton, jets, and missing transverse momentum at 13 TeV with the CMS experiment, J. High Energy Phys. 05 (2020) 032.
[94] G. Aad *et al.* (ATLAS Collaboration), Search for a scalar partner of the top quark in the all-hadronic $t\bar{t}$ plus missing transverse momentum final state at $\sqrt{s} = 13$ TeV with the ATLAS detector, Eur. Phys. J. C **80**, 737 (2020).
[95] G. Aad *et al.* (ATLAS Collaboration), Search for new phenomena with top quark pairs in final states with one lepton, jets, and missing transverse momentum in pp collisions at $\sqrt{s} = 13$ TeV with the ATLAS detector, J. High Energy Phys. 04 (2021) 174.
[96] G. Aad *et al.* (ATLAS Collaboration), Search for new phenomena in events with two opposite-charge leptons, jets and missing transverse momentum in pp collisions at $\sqrt{s} = 13$ TeV with the ATLAS detector, J. High Energy Phys. 04 (2021) 165.
[97] G. Aad *et al.* (ATLAS Collaboration), Search for new phenomena in final states with b-jets and missing transverse momentum in $\sqrt{s} = 13$ TeV pp collisions with the ATLAS detector, J. High Energy Phys. 05 (2021) 093.
[98] M. Aaboud *et al.* (ATLAS Collaboration), Search for photonic signatures of gauge-mediated supersymmetry in 13 TeV pp collisions with the ATLAS detector, Phys. Rev. D **97**, 092006 (2018).
[99] A. Tumasyan *et al.* (CMS Collaboration), Combined searches for the production of supersymmetric top quark partners in proton–proton collisions at $\sqrt{s} = 13$TeV, Eur. Phys. J. C **81**, 970 (2021).
[100] G. Aad *et al.* (ATLAS Collaboration), Searches for new phenomena in events with two leptons, jets, and missing transverse momentum in 139 fb^{-1} of $\sqrt{s} = 13$ TeV pp collisions with the ATLAS detector, Eur. Phys. J. C **83**, 515 (2023).
[101] G. Aad *et al.* (ATLAS Collaboration), Search for new phenomena in events with an energetic jet and missing transverse momentum in pp collisions at $\sqrt{s} = 13$ TeV

with the ATLAS detector, Phys. Rev. D **103**, 112006 (2021).
[102] S. Chatrchyan *et al.* (CMS Collaboration), Search for top squarks in R-parity-violating supersymmetry using three or more leptons and B-tagged jets, Phys. Rev. Lett. **111**, 221801 (2013).
[103] M. Aaboud *et al.* (ATLAS Collaboration), Search for electroweak production of supersymmetric particles in final states with two or three leptons at $\sqrt{s} = 13$ TeV with the ATLAS detector, Eur. Phys. J. C **78**, 995 (2018).
[104] ATLAS Collaboration, Search for the direct production of charginos and neutralinos in final states with tau leptons in $\sqrt{s} = 13$ TeV pp collisions with the ATLAS detector, Report No. ATLAS-CONF-2022-042, 2022.
[105] G. Aad *et al.* (ATLAS Collaboration), Search for direct production of electroweakinos in final states with one lepton, missing transverse momentum and a Higgs boson decaying into two b-jets in pp collisions at $\sqrt{s} =$ 13 TeV with the ATLAS detector, Eur. Phys. J. C **80**, 691 (2020).
[106] G. Aad *et al.* (ATLAS Collaboration), Search for charginos and neutralinos in final states with two boosted hadronically decaying bosons and missing transverse momentum in pp collisions at $\sqrt{s} = 13$ TeV with the ATLAS detector, Phys. Rev. D **104**, 112010 (2021).
[107] A. Tumasyan *et al.* (CMS Collaboration), Search for electroweak production of charginos and neutralinos at $\sqrt{s} =$ 13 TeV in final states containing hadronic decays of WW, WZ, or WH and missing transverse momentum, Phys. Lett. B **842**, 137460 (2023).
[108] A. Tumasyan *et al.* (CMS Collaboration), Search for electroweak production of charginos and neutralinos in proton-proton collisions at $\sqrt{s} = 13$ TeV, J. High Energy Phys. 04 (2022) 147.
[109] A. Hayrapetyan *et al.* (CMS Collaboration), Combined search for electroweak production of winos, binos, higgsinos, and sleptons in proton-proton collisions at $\sqrt{s} = 13$ TeV, Phys. Rev. D **109**, 112001 (2024).
[110] G. Aad *et al.* (ATLAS Collaboration), Statistical combination of ATLAS run 2 searches for charginos and neutralinos at the LHC, Phys. Rev. Lett. **133**, 031802 (2024).
[111] G. Aad *et al.* (ATLAS Collaboration), Search for pair production of higgsinos in events with two Higgs bosons and missing transverse momentum in $\sqrt{s} = 13$ TeV pp collisions at the ATLAS experiment, Phys. Rev. D **109**, 112011 (2024).
[112] A. M. Sirunyan *et al.* (CMS Collaboration), Search for additional neutral MSSM Higgs bosons in the $\tau\tau$ final state in proton-proton collisions at $\sqrt{s} = 13$ TeV, J. High Energy Phys. 09 (2018) 007.
[113] G. Aad *et al.* (ATLAS Collaboration), Search for heavy Higgs bosons decaying into two tau leptons with the ATLAS detector using pp collisions at $\sqrt{s} = 13$ TeV, Phys. Rev. Lett. **125**, 051801 (2020).
[114] F. Staub, SARAH, arXiv:0806.0538.
[115] F. Staub, Automatic calculation of supersymmetric renormalization group equations and self energies, Comput. Phys. Commun. **182**, 808 (2011).
[116] F. Staub, Exploring new models in all detail with SARAH, Adv. High Energy Phys. **2015**, 840780 (2015).
[117] W. Porod, SPheno, a program for calculating supersymmetric spectra, SUSY particle decays and SUSY particle production at $e^+ e^-$ colliders, Comput. Phys. Commun. **153**, 275 (2003).
[118] W. Porod and F. Staub, SPheno 3.1: Extensions including flavour, CP-phases and models beyond the MSSM, Comput. Phys. Commun. **183**, 2458 (2012).
[119] W. Porod, F. Staub, and A. Vicente, A Flavor Kit for BSM models, Eur. Phys. J. C **74**, 2992 (2014).
[120] S. Navas *et al.* (Particle Data Group), Review of particle physics, Phys. Rev. D **110**, 030001 (2024).
[121] M. Drees, S. Pakvasa, X. Tata, and T. ter Veldhuis, A supersymmetric resolution of solar and atmospheric neutrino puzzles, Phys. Rev. D **57**, R5335 (1998).
[122] H. K. Dreiner, Y. S. Koay, D. Köhler, V. M. Lozano, J. Montejo Berlingen, S. Nangia, and N. Strobbe, The ABC of RPV: Classification of R-parity violating signatures at the LHC for small couplings, J. High Energy Phys. 07 (2023) 215.
[123] A. Choudhury, A. Mondal, S. Mondal, and S. Sarkar, Improving sensitivity of trilinear R-parity violating SUSY searches using machine learning at the LHC, Phys. Rev. D **109**, 035001 (2024).
[124] A. Choudhury, A. Mondal, S. Mondal, and S. Sarkar, Slepton searches in the trilinear RPV SUSY scenarios at the HL-LHC and HE-LHC, Eur. Phys. J. Special Topics **233**, 2163 (2024).
[125] P. Bandyopadhyay and B. Bhattacherjee, Boosted top quarks in supersymmetric cascade decays at the LHC, Phys. Rev. D **84**, 035020 (2011).
[126] A. Choudhury and A. Datta, New limits on top squark NLSP from LHC 4.7 fb^{-1} data, Mod. Phys. Lett. A **27**, 1250188 (2012).
[127] A. Chakraborty, D. K. Ghosh, S. Mondal, S. Poddar, and D. Sengupta, Probing the NMSSM via Higgs boson signatures from stop cascade decays at the LHC, Phys. Rev. D **91**, 115018 (2015).
[128] P. Konar, T. Mondal, and A. K. Swain, Demystifying the compressed top squark region with kinematic variables, Phys. Rev. D **96**, 095011 (2017).
[129] C. Han, J. Ren, L. Wu, J. M. Yang, and M. Zhang, Top-squark in natural SUSY under current LHC Run-2 data, Eur. Phys. J. C **77**, 93 (2017).
[130] N. Chamoun, H. K. Dreiner, F. Staub, and T. Stefaniak, Resurrecting light stops after the 125 GeV Higgs in the baryon number violating CMSSM, J. High Energy Phys. 08 (2014) 142.
[131] S. Chakraborty, A. Datta, K. Huitu, S. Roy, and H. Waltari, Light top squarks in $U(1)_R$-lepton number model with a right handed neutrino and the LHC, Phys. Rev. D **93**, 075005 (2016).
[132] S. P. Das, A. Datta, and S. Poddar, Top squark and neutralino decays in a R-parity violating model constrained by neutrino oscillation data, Phys. Rev. D **73**, 075014 (2006).

[133] A. Datta and S. Poddar, Probing R-parity violating models of neutrino mass at the LHC via top squark decays, Phys. Rev. D **79**, 075021 (2009).

[134] R. Bose, A. Datta, A. Kundu, and S. Poddar, LHC signatures of neutrino mass generation through R-parity violation, Phys. Rev. D **90**, 035007 (2014).

[135] A. Datta and B. Mukhopadhyaya, Are messages of R-parity violating supersymmetry hidden within top quark signals?, Phys. Rev. Lett. **85**, 248 (2000).

[136] D. Restrepo, W. Porod, and J. W. F. Valle, Broken R-parity, stop decays, and neutrino physics, Phys. Rev. D **64**, 055011 (2001).

[137] Z. Marshall, B. A. Ovrut, A. Purves, and S. Spinner, Spontaneous *R*-parity breaking, stop LSP decays and the neutrino mass hierarchy, Phys. Lett. B **732**, 325 (2014).

[138] Z. Marshall, B. A. Ovrut, A. Purves, and S. Spinner, LSP squark decays at the LHC and the neutrino mass hierarchy, Phys. Rev. D **90**, 015034 (2014).